UNDERSTANDING SURFACE FORCES AND INTERACTION MECHANISMS IN MINERAL FLOTATION BY ATOMIC FORCE MICROSCOPY

by

Liyuan Feng

A thesis submitted in partial fulfillment of the requirements for the degree of

Master of Science

in

Chemical Engineering

Department of Chemical and Materials Engineering
University of Alberta

Abstract

Bubble-particle interactions are ubiquitous and crucial to mineral flotation. The bubble-particle attachment process is mainly governed by three surface forces: van der Waals (vdW), electrical double-layer (EDL), and hydrophobic (HB) forces. Atomic Force Microscopy (AFM) has become the most prominent technique to measure the surface forces due to its versatility and pico-Newton resolution. By anchoring a micron-sized oil droplet or bubble onto a tipless AFM cantilever, the so-called AFM bubble probe allows for accurate force measurement involving deformable bodies. In this study, a number of force measurements were performed with the advantage of the AFM bubble probe technique to understand the surface forces in mineral flotation. The interaction mechanisms were underpinned by the well-established Stokes-Reynolds-Young-Laplace (SRYL) model.

Molybdenite (MoS_2) is a mineral that has drawn great interest because of its potential application in various fields. To facilitate the flotation of molybdenite, the mineral pulp is commonly treated with nonpolar oil additives to promote hydrophobicity and to form an oil bridge between ultrafine molybdenite particles for agglomeration. In this study, dodecane was chosen as a model oil to investigate the flotation mechanisms of molybdenite with nonpolar oil. The interaction forces between a micrometer-sized dodecane droplet and the molybdenite basal plane in various electrolyte solutions were directly measured by the atomic force microscope droplet probe technique. The effects of added salts, ionic strength, and solution pH on interaction forces were evaluated by considering van der Waals, electrical double-layer (EDL), and hydrophobic forces. The experimentally measured force curves were found to agree well with the Reynolds lubrication model and the augmented Young-Laplace equation. The results show that the competition between repulsive EDL forces and attractive hydrophobic forces was directly responsible for oil-molybdenite attachment behavior. High pH and low salinity (<24 mM NaCl) led to strong repulsive EDL forces, which stabilized the interaction and prevented the attachment of oil to molybdenite. Both low pH and high salinity facilitated the attachment of oil to molybdenite through the depression of EDL force, allowing attractive hydrophobic force to dominate. The hydrophobic attraction was

quantified with an exponential decay length of 1.0 ± 0.1 nm. Furthermore, calcium ions decreased the magnitude of the surface potentials of both oil and molybdenite more than that seen with the same ionic strength of sodium ions, suggesting the suppressed EDL repulsion. This study provides quantitative information about the surface forces between oil and the molybdenite basal plane and an improved understanding of the fundamental interaction mechanisms governing molybdenite recovery by mineral flotation.

The wettability and surface potential of millerite (NiS) under pH 4 and pH 12 were investigated. Experimental data suggested that elemental sulfur and/or polysulfde (S_n^{2-}) formed under acidic condition (pH 4) rendered the millerite surface hydrophobic and favored the bubble-millerite attachment, where HB force dominated the interaction. In contrast, hydrophilic Ni(OH)2 formed under pH 12, acted as a passivation layer, and caused the millerite surface to become less hydrophobic. Thus repulsive EDL force inhibited the bubble-millerite attachment.

The influence of oxidation using H_2O_2 solution on pentlandite was studied in borax buffer solution. The additive of H_2O_2 did not alter the hydrophilicity but increased the surface roughness by introducing nanoscale asperities onto pentlandite. Combined with PIBX treatment, pentlandite showed chemical heterogeneity and partial hydrophobicity but still allowed for bubble attachment. When pentlandite underwent direct xanthate treatment, it showed less chemical heterogeneity and stronger hydrophobicity, and micron-sized bubble attachment could readily be induced as desired. The characteristic lengths of HB forces were found to be 0.9 ± 0.1 nm and 1.2 ± 0.1 nm for H_2O_2-PIBX treated pentlandite, and PIBX treated pentlandite, respectively. In addition, the chemical properties of pentlandite was well-characterized at nanoscale by adhesion force map.

This study provides quantitative information about the surface forces between oil/bubble and mineral surfaces and an improved understanding of the fundamental interaction mechanisms in mineral flotation.

Preface

This thesis is composed of original work by Liyuan Feng and parts of research collaboration. The following is a statement of contributions made to collaborative work contained in this thesis:

- Chapter 1 : Introduction is an original work by Liyuan Feng.
- Chapter 2 of this thesis has been pulished as: "Unraveling Interaction Mechanisms between Molybdenite and a Dodecane Oil Droplet Using Atomic Force Microscopy", co-authored by Liyuan Feng, Rogerio Manica, James S. Grundy, and Qingxia Liu in: *Langmuir* **2019**, 35, 18, 6024-6031. I was reponsible for sample preparation, data collection, data analysis, and manuscript composition. Dr. Manica contributed to the Matlab program and manuscript revision. Dr. Grundy contributed to manuscript edits. Dr. Liu was the supervisory author providing the concept formation.
- Chapter 3 contains the results of wettability of millerite in different pH. Dr. Jing Liu prepared the millerite sample. AFM force measurements and data analysis are my original work.
- Chapter 4 provides the effect of xanthates and H_2O_2 oxidation on the interaction between bubble and pentlandite. Chao Qi was involved in concept formation and sample preparation. I was responsible for data collection, data analysis, and manuscript composition.
- Chapter 5,: Conclusion is original work by Liyuan Feng. No part of this thesis has previously been published.
- Chapter 2 was presented at the 9th Australian Colloid & Interface Symposium in Hobart, Tasmania, Australia.

Dedicated to Dad and Mom, Zhujun and Hezhen,
whose support and love is what has made me who I am.

Acknowledgements

First and foremost, I would like to thank my supervisor, Dr. Qingxia (Chad) Liu, for his patient and valuable guidance, for providing me with opportunities to find my own interests. My sincere thanks goes to Dr. Ruan Chi for his inspiration. I am indebted to Dr.Rogerio Manica, for his continuous guidance on my research. I have much appreciation for my colleagues: Dr. Jing Liu, Dr. Bo Liu, Dr. Nguyen Thuy Vu Truong, Bailin Xiang, Chao Qi, Hanrui Zheng, Mingda Li, Hao Huang for your productive discussions and enjoyable lunch time. Mr. Hope Huang is thanked for drawing the AFM schematic. The financial support from the Natural Sciences and Engineering Research Council of Canada (NSERC)-Industrial Research Chair Program in Oil Sands Engineering, a NSERC Discovery Grant, a NSERC Strategic Project Grant, and The Canadian Centre for Clean Coal/Carbon and Mineral Processing Technologies (C^5MPT) are greatly appreciated. Finally, I would like to express my deepest gratitude to my parents and other family members for their unconditional love and support. Special thanks goes to Yijia Sun. Thank you for your companionship, encouragement, and trust throughout these years.

Contents

List of Figures

List of Tables

List of Symbols

Symbol	Description	Units
A	Hamaker constant	
D_0	Decay length of hydrophobic force	
E	Capture efficiency	
E_a	Attachment efficiency	
E_c	Collision efficiency	
E_s	Stability efficiency	
R	Radius of oil droplet	
T	Temperature	
$X(t)$	Separation between the cantilever and sample surface	
Π	Disjoining pressure	
Ψ	Surface potential	
κ	Inverse of the Debye length	
μ	Viscosity of aqueous solution	
ρ_0	Number concentration of the bulk electrolyte	
σ	Dodecane/water interfacial tension	
θ	Contact angle	
ε	Aqueous dielectric permittivity	
ε_0	Vacuum permittivity	
e	Elementary charge	
h	Water film thickness	
k_B	Boltzmann constant	

Symbol	Description	Units
p	Hydrodynamic pressure	
r	Radial coordinate	
t	Time	
Acronyms		
AFM	Atomic Force Microscopy	
EDL	Electrical Double Layer	
EDLVO	Extend Derjaguin-Landau-Verwey-Overbeek	
EDS	Energy Disperse X-ray Spectra	
HB	Hydrophobic	
LVDT	Linear Variable Differential Transformer	
PIBX	Potassium isobutyl xanthate	
RMS	Root Mean Square	
SEM	Scanning Electron Microscope	
SRYL	Stokes-Reynolds-Young-Laplace	
TPCL	Three Phase Contact Line	
vdW	van der Waals	
XPS	X-ray Photoelectron Spectroscopy	

Chapter 1

Introduction

1.1 Background and motivations

Mineral flotation is a process that separates valuable minerals from gangue mineral based on the differences in the hydrophobicity of mineral particles. The centerpiece of this process is capturing hydrophobic particles by rising bubbles and leaving the hydrophilic particles suspended in the pulp. The bubble-particle interactions can be resolved into three sub-processes: collision, attachment, and detachment. Thus, the final capture outcome is the consequences of these three sub-processes:[1]

$$E = E_c \times E_a \times E_s \tag{1.1}$$

where E is the capture efficiency, E_c is the collision efficiency, E_a is the attachment efficiency, and E_s is the stability efficiency of the bubble-particle aggregate.

Each sub-process is governed by different factors. First, the degree of mobility of the bubble surface and the inertial forces playing on the particles from hydrodynamics in the flotation cell conjointly control the collision efficiencies. Second, when bubble and

mineral particles are brought in proximity (below a few hundred nanometer), surface chemistry, surface roughness, water chemistry, and colloidal forces are the main factors that influence the attachment efficiency. Lastly, shear forces and hydrodynamic forces may drag air bubbles away from the mineral particles where only capillary forces hold the bubble-particles aggregates together.[2, 3] Since this introduction focuses on the attachment efficiency, comprehensive literature reviews pertaining to collision and detachment efficiencies are summarized in detail elsewhere.[4–6]

To improve the bubble-particle attachment process, many additives are used to enhance the hydrophobicity of valuable minerals which further increase the attractive forces between bubble and mineral particles. Hydrocarbon oils such as kerosene and diesel oil encourage the agglomerates of molybdenite particles and thus promote the flotation. Similarly, thiol-type collectors like xanthates can adsorb on sulfide minerals by chemisorption and render them hydrophobic. As for the surface forces for bubbe-particle attachment, van der Waals (vdW), electrical double-layer (EDL), and hydrophobic (HB) forces are the main roles that come into play at nanometer separation. Ideally, the hydrophobic force between air bubble and hydrophobic particles will dominate the colloidal force and induce the attachment. However, the repulsive electrical double layer forces arising from the electrolyte in process water may overcome the attractive hydrophobic forces and reduce attachment efficiency. It is also reported that high saline water prevented the xanthate adsorption onto mineral due to competitive adsorption thereby decreasing the hydrophobicity of the mineral particles.[7] Another major challenge for sulfide mineral is oxidation.[8–12] Diversity of oxidation products results in different surface chemistry and thus distinct flotation recovery. Oxidation of galena (PbS) allows for collectless flotation of galena,[13] whereas the natural hydrophobicity of molybdenite (MoS_2) can be altered

because of the soluble oxidation products.[14]

1.2 Approaches to understand the bubble-particle attachment

The bubble-particle attachment can be further divided into several steps: (1) the water film between air bubble and particle becomes thinning until the so-called critical film thickness (the minimum film thickness before rupture), (2) the water film ruptures and Three Phase Contact Line (TPCL) forms, (3) TPCL expands until forming a stable wetting perimeter.[15] To understand each step, various experimental approaches have been developed. During early 1930s, Sven-Nilsson [16] introduced the concept of induction time, which is the time required for step one. In 2003, Gu et al. [17] refined the setup for induction time measurement. A speaker drum was utilized to control the approach velocity and displacement of bubble. A CCD camera along with a real-time analysis system accurately controlled the bubble size and produced the results at a resolution of 0.1 ms. Similarly, by recording and analyzing the bubble-mineral interaction images, High-Speed Video Microscopy (HSVM) was able to determine the liquid film drainage rates and contact angles of a 1-mm diameter air bubble on sphalerite and pyrite.[18] These macroscopic approaches offer direct observations of bubble deformation behavior yet quantitative understanding of surface force is absent.

The experimental techniques developed for precise characterization of bubble-particle attachment fall into two categories: film drainage observation and force measurement, where hydrodynamic information can be extracted from the optical interference fringes in film drainage profile and surface force variation can be well characterized from force measurement. Generally, a monochromatic interferometry equipped with a high-speed camera allows for the observation of thin film, and Atomic Force Microscopy (AFM)

facilitates the force measurement between various surfaces or interfaces at nanometer resolution. Force measurement involving deformable interfaces will be discussed here.

In 1994, Ducker et al. [19] first studied bubble-surface interaction by approaching a micron-sized silica sphere toward an air bubble immobilized on the bottom. An attractive force between the hydrophobic silica sphere and air bubble that the classic Derjaguin-Landau-Verwey-Overbeek (DLVO) theory could not predict was observed. During early 2000s, Dagastine et al. [20] fabricated a tipless AFM cantilever with a gold patch on the end. After the cantilever being hydrophobized by thiol solution, an air bubble with radius of $50 \sim 60$ μm can be readily anchored and functioned as the probe. The theoretical model established by Chan et al. [21], the Stokes-Reynolds-Young-Laplace (SRYL) model, made the quantitative analysis for bubble-surface interaction possible.[22] The advantage of this methodology lies in the precise measurement of hydrophobic force. Thus, it has been effectively employed for bubble-mineral interactions.[23, 24] The merit of this approach has also been recognized when including other deformable objects: bubble-bubble, drop-drop, and bubble-drop.[25–31] Significant effort has been delicated to develop novel methods to measure both film profile and force simultaneously. Recently, Atomic Force Microscopy combined with reflection interference contrast microscopy (AFM-RICM) has produced some promising results.[32]

1.3 Objectives and scope of the Thesis

The ability of AFM droplet/bubble probe technique has been extended to precise interaction force measurement between oil droplet/bubble and mineral surfaces. The schematic illustration of droplet probe is depicted in Figure 1.1. This technique is especially demanding, since roughness on the surfaces of interest may mislead the attachment results. Hereby

a series of AFM experiments were initiated on three minerals: molybdenite (where basal planes are molecularly smooth), millerite (RMS roughness of the cleaved surface is 2.4 nm), and pentlandite (RMS roughness of the hand-polished sample is 1.6 nm). Fundamental investigation on the surface forces and interaction mechanisms is highly required and beneficial to the original knowledge in mineral flotation. Accordingly, the objectives of present study fall into six points:

1. To investigate the interaction mechanisms for the interaction between oil droplet and molybdenite basal plane in aqueous solutions.

2. To quantitatively clarify the main driving forces involved in the oil-molybdenite interaction with varying pH, salt concentration, and Ca^{2+} ions.

3. To predict the favorable conditions for the oil droplet attachment to molybdenite.

4. To determine the wettability and surface potential of millerite at different pH.

5. To study the effect of oxidation induced by H_2O_2 on bubble-pentlandite interaction at pH 9.3.

6. To examine the topography and chemical properties of pentlandite after H_2O_2-PIBX and PIBX conditioning.

1.4 Structure of the thesis

Chapter 1 provides an overview of the background information, problem statement, and the objectives of the thesis. Chapter 2 investigates the interacion forces between a micrometer-sized dodecane droplet and the molybdenite basal plane in various electrolyte solutions by the atomic force microscope droplet probe technique. A version of this chapter

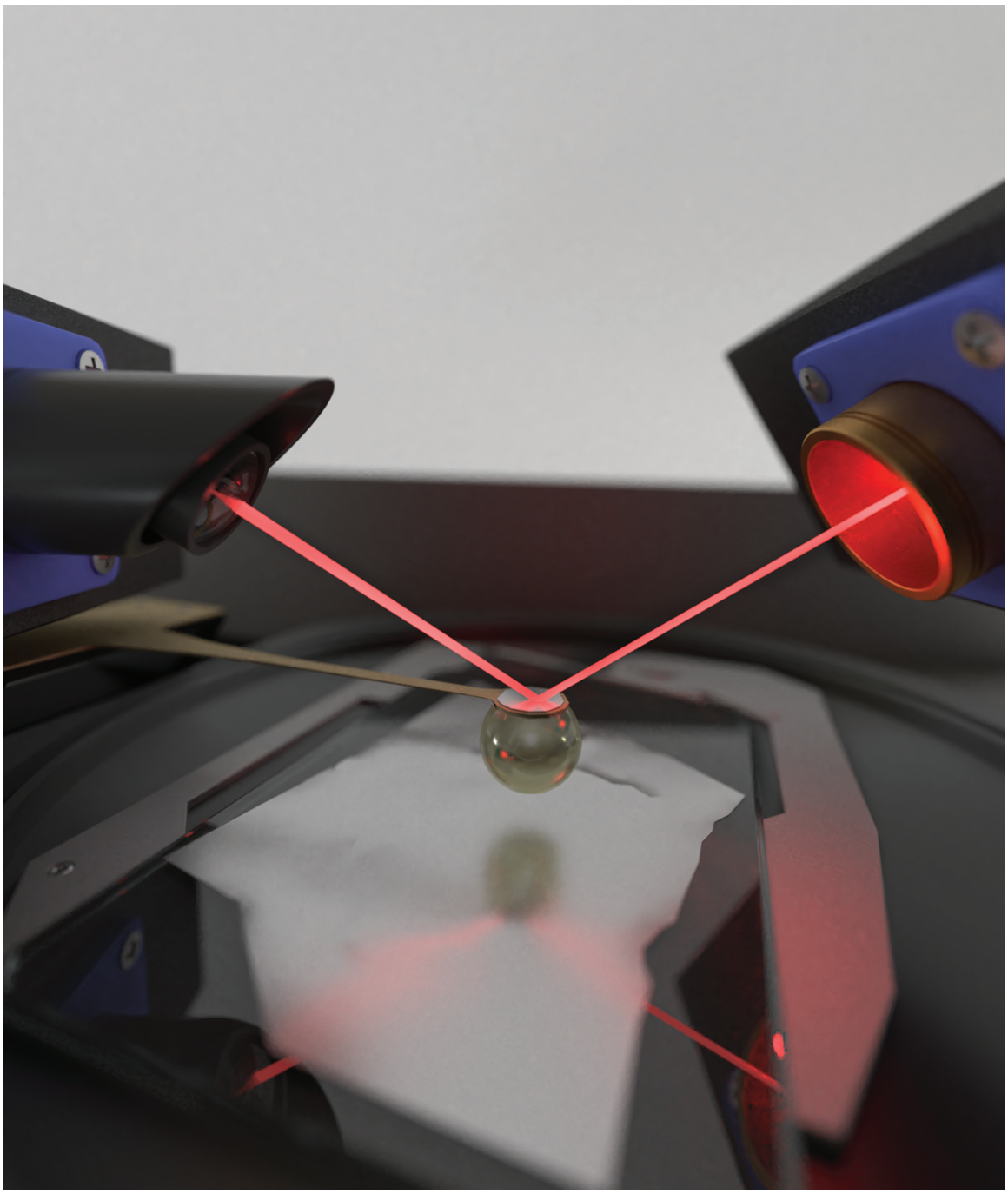

Figure 1.1: Schematic representation of the AFM droplet probe technique

has been published as: Liyuan Feng, Rogerio Manica, James S. Grundy, and Qingxia Liu, Unraveling Interaction Mechanisms between Molybdenite and a Dodecane Oil Droplet Using Atomic Force Microscopy. *Langmuir* **2019**, 35, 18, 6024-6031. Chapter 3 illustrates the effect of pH on the surface potential and wettability of millerite in 10 mM KCl solution. Chapter 4 discusses the impact of oxidation induced by H_2O_2 on bubble-pentlandite interaction at pH 9.3. In Chapter 5, the conclusions of this thesis and recommendations for future work are presented.

Chapter 2

Unraveling Interaction Mechanisms between Molybdenite and a Dodecane Oil Droplet Using Atomic Force Microscopy

2.1 Introduction

In recent years, molybdenite (MoS_2) has emerged as a promising material for a wide range of applications due to its semiconducting electric properties. The molybdenite mineral is composed of a multitude of stacked MoS_2 monolayers, which can be separated to yield thin sheets. The exposed flat surfaces are known as the basal plane of the mineral and are accepted as molecularly smooth.[24] Molybdenite is extracted from natural ores by froth flotation.[33] The primary objective of froth flotation is the selective capture of valuable mineral particles by bubbles. Surface forces contributing to mineral capture by bubbles, including van der Waals (vdW), electrical double layer (EDL), hydrophobic (HB), and hydration forces, are influenced by many physicochemical factors, such as water chemistry, surface wettability, and surface roughness. When hydrodynamic forces are sufficient to bring a particle very close to a bubble and overcome any repulsive surface forces, the water film between the bubble and particle ruptures and bubble-particle capture occurs.[33] To increase the extent of mineral recovery by flotation, an oily collector is added to the mineral pulp before the introduction of air bubbles. The collector adsorbs to and coats the molybdenite surface, which enhances the attractive surface force between the bubble molybdenite and results in an increased level of agglomeration and floc-flotation, improving extraction efficiency.[34, 35] Due to their low surface energy and wide availability, nonpolar oils, such as diesel oil and kerosene, are typically chosen for this application. Although hydrophobic attraction has been confirmed by interfacial calculation as the main driving force for the attachment of oil to molybdenite, the mechanisms of interaction between oil and molybdenite are still not well understood.[36]

Considerable efforts have been made to understand the underlying mechanisms for the role of nonpolar oils in mineral flotation. Liu et al. [37] studied the interfacial interactions

between quarts particles and oil droplets on the basis of the extend Derjaguin-Landau-Verwey-Overbeek (EDLVO) theory. After calculation of the contributions of vdW, EDL, HB, and hydrocarbon chain association interactions, hydrophobic interaction was found to dominate particle-oil attachment. Similar conclusions have been reached in studies regarding flotation of various other minerals.[36, 38, 39]

To fully understand the fundamentals of the hydrophobic interaction, several studies examined different techniques for force measurements between hydrophobic surfaces prepared by different methods.[40–44] One of the proposed models for the hydrophobic interaction mechanism is that water molecules rearrange themselves with surrounding hydrophobic surfaces to favor hydrogen bonding.[45] The range of hydrophobic forces is exhibited as an exponential decay length of 0.3-1.0 nm.[46]

A nanomechanical technique known as an atomic force microscope (AFM) droplet probe was developed by Dagastine et al. [20]. In this method, a gold patch on a tipless cantilever can anchor an air bubble or oil droplet, which then function as the probe tip. In addition to directly measuring the interaction forces involving deformable interfaces, the AFM droplet probe technique offers a few distinct advantages. Due to the smooth surface of the droplet, reliable and reproducible results may be obtained, as compared to the results with a sharp tip. Furthermore, with a large contact area to the test surface, the deformable interface of the droplet probe provides very sensitive results. On the basis of the Reynolds lubrication theory and the augmented Young-Laplace equation, a theoretical model called the Stokes-Reynolds-Young-Laplace (SRYL) model was established.[21] The AFM droplet probe technique coupled with the SRYL model provides many advantages in quantitatively understanding surface forces in bubble and droplet systems, such as the interaction between bubbles and hydrophobic surfaces,[22, 47] deformable droplets,[25, 48]

and gas bubbles[49]. Recently, this method was shown to be a powerful tool for elucidating the mechanisms behind enhanced oil recovery,[50] mineral flotation,[23, 24, 51] and food emulsions.[52, 53]

The purpose of this work is to investigate the role of nonpolar oil in the flotation of molybdenite. Dodecane, a key component of petroleum diesel, was chosen as a model oil. For the first time, the droplet probe AFM technique was employed to directly measure the interaction forces between a micrometer-sized dodecane droplet and a molybdenite basal plane under different aqueous solutions in the absence of a surfactant. Experimental results presented in this study were interpreted using the SRYL model. The effects of solution pH, ionic strength, and added salts were evaluated by accounting for vdW, EDL, and HB interaction forces. The findings yield fundamental insight regarding the mechanism of oil agglomeration flotation of molybdenite and could also have broad implications for oil agglomeration techniques for other minerals and resources, such as quarts, coal, or hematite.

2.2 Experimental section

2.2.1 Materials and methods

Dodecane ($C_{12}H_{26}$, anhydrous, $\geq$ 99%, Sigma), ethanol(for high-performance liquid chromatography, Acros Organics), and 1-dodecanethiol ($\geq$ 98%, Sigma) were used without further purification. Molybdenite was provided by the Wolfram mine site (Queensland, Australia). Sodium hydroxide (NaOH, ACS reagent grade, Fisher Scientific) and hydrochloric acid (HCl, ACS reagent grade, Fisher Scientific) were used to adjust the solution pH. All pH measurements were taken using a Fisherbrand accumet XL 150 pH meter with a Fisherbrand accuTupH rugged bulb pH electrode. The electrode was calibrated daily

before use with buffer sachets (Mettler Toledo) of pH 4.01, 7.00, and 10.00. Sodium chloride (NaCl, ACS reagent grade, Fisher Scientific) and calcium chloride dihydrate ($CaCl_2$, ACS reagent grade, Fisher Scientific) were purified via recrystallization and calcination at 550 °C for 6 h to remove organic contaminants and used immediately. All aqueous solutions were prepared using Milli-Q water with a resistivity of 18.2 m$\Omega \cdot$ cm from a Barnstead Nanopure system (Thermo Fisher Scientific). All glassware was cleaned by being repeatedly rinsed with toluene, acetone, Milli-Q water, and acetone again and then dried with high-purity nitrogen.

The dodecane/water interfacial tension was measured using the pendant drop method with a Theta Optical Tensiometer T200 (Biolin Scientific, Stockholm, Sweden) at room temperature. Contact angles formed by sessile drops were measured using the same system. A glass cuvette was first filled with the target salt solution. Next, a dodecane oil drop was formed through a custom-made upward-bent needle on a Hamilton glass syringe. The shape of the oil drop was recorded continuously for 1 h. For dodecane drops in a salt solution, an interfacial tension of 45 ± 0.5 mN/m was obtained over the electrolyte concentration range used, which indicated the absence of surface-active components.

2.2.2 Zeta potential measurement

ζ potential measurements of dodecane in different solutions were carried out using a Zetasizer Nano ZSP (Malvern Instruments). Emulsions were obtained by sonicating a mixture of 2 vol% dodecane in an electrolyte solution at the desired pH.

2.2.3 Force measurement

All force measurements between a dodecane droplet and the molybdenite basal plane in aqueous solutions were taken using an MFP-3D AFM system (Asylum Research, Santa

Barbara, CA) couple with a Carl Zeiss Axiovert 200 inverted microscope. A portless fluid cell was used to reduce the risk of fluid leakage. A custom-made rectangular silicon tipless AFM cantilever with a circular gold patch (65 μm in diameter) at the end was used in this study. The cantilever was further hydrophobized by immersion in a 10 mM 1-dodecanethiol ethanolic solution overnight. Adsorption of the 1-dodecanethiol monolayer to the gold patch ensured that the oil droplet was immobilized at the end of the cantilever throughout the experiment. Prior to the oil droplet being anchored, the spring constant of the cantilever was determined by the Hutter and Bechhoefer thermal spectrum method and found to range from 0.2 to 0.3 N/m.[54] A small piece of molybdenite and a silica wafer were glued on a glass slide with epoxy resin and placed into the fluid cell. Prior to AFM force measurements, molybdenite was cleaved using Scotch tape to expose a fresh basal plane. Two mililiters of the salt solution was then slowly added to the fluid cell followed by injection of oil droplets onto the silica wafer by a custom-made ultrasharp pipet. The tipless AFM cantilever was wetted with the target salt solution prior to being mounted on the cantilever holder. After the holder had been installed on the AFM head, the AFM head was lowered slowly into the fluid cell. Then the cantilever was positioned over an oil droplet of the desired size (50 $\sim$ 60 μm radius) as monitored with the top-view camera, and the cantilever was lowered carefully to pick up the oil droplet. The size of the oil droplet was determined through the bottom window of the fluid cell using the inverted microscope. The oil droplet probe was then brought over the molybdenite surface, and force measurements were conducted under a trigger point of 20 nN or until oil attachment occurred. The drive velocity was fixed at 1 μm/s to minimize hydrodynamic effects. To confirm reproducibility, force measurements were performed at least five times for each condition using different oil droplets at different sites on the surface. A schematic of the

experimental setup is shown in Figure 2.1.

While the sample surface was driven toward or away from the cantilever, the deflection and motion of the cantilever were detected and recorded as a voltage change by the photodiode. The detector sensitivity was determined by a Linear Variable Differential Transformer (LVDT) within the region where the voltage signal was proportional to the displacement of the cantilever. The electrical signal was then converted to the corresponding interaction forces between the oil droplet and sample surface according to Hooke's law.

2.2.4 Theoretical calculation

The Reynolds lubrication model and the augmented Young-Laplace equation were employed to analyze the experimental data. This approach has been widely used to calculate the dynamic force between droplet/bubble and surfaces since it was developed.[21] The evolution of the thin film drainage process can be described by the Stokes - Reynolds model as

$$\frac{\partial h}{\partial t} = \frac{1}{12\mu r}\frac{\partial}{\partial r}\left(rh^3\frac{\partial p}{\partial r}\right) \tag{2.1}$$

where h is the water film thickness, r is the radial coordinate, μ is the viscosity of the aqueous solution, and p is the hydrodynamic pressure in the thin film between the oil droplet and surface. An immobile boundary condition was assumed at both the oil-water and oil-molybdenite interfaces.[55]

The mathematical description of the deformation of the drop caused by disjoining pressure Π and hydrodynamic pressure is based on the augmented Young Laplace equation.

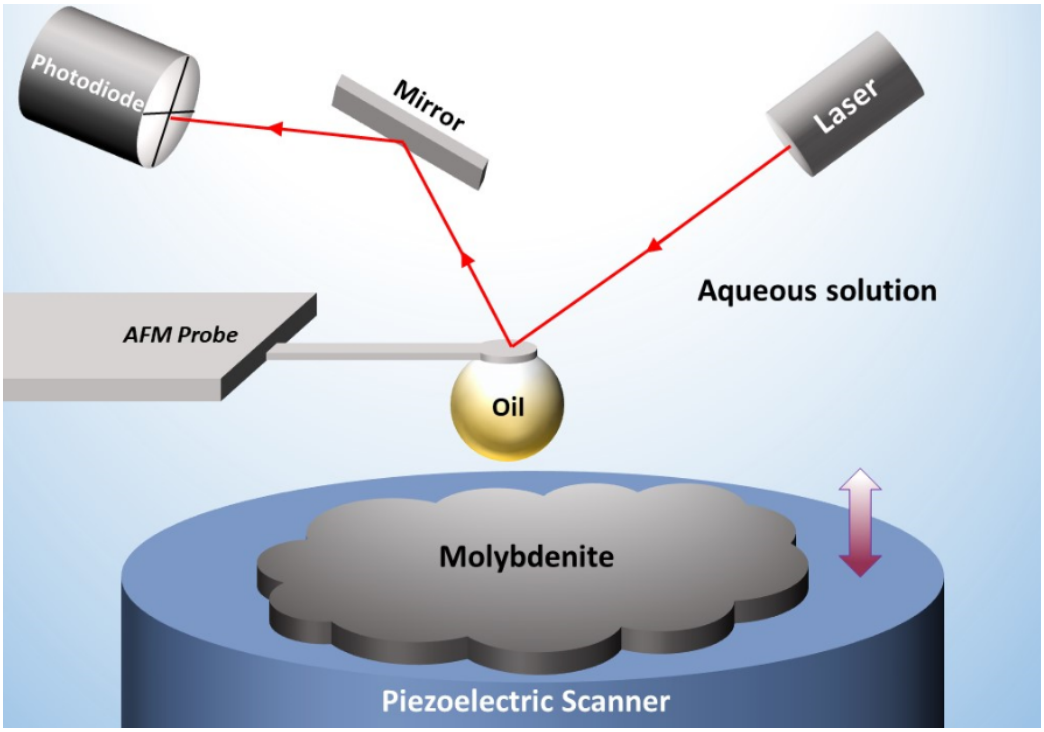

Figure 2.1: Schematic diagram of typical force measurement between an oil droplet and the molybdenite basal plane in an aqueous solution using the AFM droplet probe technique.

$$\frac{\sigma}{2r}\frac{\partial}{\partial r}\left(r\frac{\partial h}{\partial r}\right) = \frac{2\sigma}{R} - \Pi - p \tag{2.2}$$

where σ is the dodecane/water interfacial tension and R is the radius of the oil droplet. Equation (2.1) and Equation (2.2) constitute the SRYL model.

In this work, three major components of disjoining pressure were considered: van der Waals (vdW), electrical double-layer (EDL) assuming constant potential (the prediction based on constant charge boundary conditions is performed and found to have a weak influence on the attachment outcome), and hydrophobic (HB) forces, namely, $\Pi = \Pi_{vdW} + \Pi_{EDL} + \Pi_{HB}$, where each contribution can be expressed as Equation (2.3), Equation (2.4), and Equation (2.5), respectively.[23]

$$\Pi_{vdW}(h) = \frac{-A}{6\pi h^3} \tag{2.3}$$

$$\Pi_{EDL}(h) = \frac{2\varepsilon_0\varepsilon\kappa^2\left[\left(e^{\kappa h}+e^{-\kappa h}\right)\Psi_O\Psi_M-\left(\Psi_O^2+\Psi_M^2\right)\right]}{\left(e^{\kappa h}-e^{-\kappa h}\right)^2} \tag{2.4}$$

where A is the Hamaker constant for the oil/water/molybdenite system, ε_0 is vacuum permittivity, ε is the aqueous dielectric permittivity, Ψ_O, and Ψ_M are the surface potentials of the oil droplet and molybdenite surfaces, respectively, and κ is the inverse of the Debye length. $\kappa = \left(\frac{2\rho_0 e^2}{\varepsilon_0\varepsilon\kappa_B T}\right)^{1/2}$, where ρ_0 is the number concentration of the bulk electrolyte and e is the elementary charge.

$$\Pi_{HB}(h) = -\frac{\sigma\left(1-\cos\theta\right)}{D_0}e^{-h/D_0} \tag{2.5}$$

where θ is the contact angle of oil on the molybdenite surface measured in aqueous electrolytes and D_0 is the decay length of hydrophobic force. The total interaction force between the oil droplet and the surface is given by the integral of the hydrodynamic and disjoining pressures over the interval $0 \leq r \leq r_{max}$ according to the Derjaguin approximation:

$$F(t) = 2\pi\int_0^\infty\left(p+\Pi\right)\mathrm{d}r \simeq 2\pi\int_0^{r_{max}}\left\{p\left(r,t\right)+\Pi\left[h\left(r,t\right)\right]\right\}r\mathrm{d}r \tag{2.6}$$

The SRYL model reqires four boundary conditions.[21] At the axis of symmetry $r = 0$, $\frac{\partial h}{\partial r} = \frac{\partial p}{\partial r} = 0$. The pressure decays as $p(r,t) \to r^{-4}$ for $r \to \infty$, which can be written as at $r = r_{max}$. Another boundary condition at $r = r_{max}$ is given as

$$\frac{\partial h\left(r_{max},t\right)}{\partial t} = \frac{\mathrm{d}X(t)}{\mathrm{d}t} - \frac{1}{2\pi\sigma}\frac{\mathrm{d}F(t)}{\mathrm{d}t}\left[1+\ln\left(\frac{r_{max}}{2R}\right)+\frac{1}{2}\ln\left(\frac{1+\cos\theta_o}{1-\cos\theta_o}\right)-\frac{2\pi\sigma}{k}\right] \tag{2.7}$$

where $X(t)$ is the separation between the cantilever and sample surface, θ_0 is the contact

angle of the oil droplet on the cantilever, and k is the spring constant of the cantilever.

2.3 Results and discussion

In this work, the interaction forces between a dodecane droplet and the molybdenite basal plane were systematically investigated at varying pHs and salt concentrations. Experimental data obtained using the AFM technique were then compared with theoretical predictions of the SRYL model to verify and quantify the individual strength of vdW, EDL, and HB forces. Finally, a stability map for oil droplet attachment or non-attachment was generated on the basis of the experimental data for the interaction between an oil droplet and the molybdenite surface.

2.3.1 Effects of pH on interaction between oil and molybdenite

A previous study found a strong pH dependence for the recovery of molybdenite at a low ionic strength of 10 mM.[56] The experiments in the work presented here were first carried out under low salinity over a pH range of $4 \sim 10$ to investigate the mechanisms of interaction between oil and molybdenite. The interaction force between a dodecane droplet and the molybdenite basal plane in a 10 mM NaCl solution at pH 10 is shown in Figure 2.2 A. The measured force as a function of time shows repulsion under a maximum normal load of 20 nN during approach and a weak attraction during retraction due to a hydrodynamic suction effect.[57] This indicates that the water film confined by the oil droplet and solid surface becomes thinner toward an equilibrium thickness, where no further thinning occurs.[58] By considering vdW, EDL, and HB interaction forces, the comparison between the theoretical calculation (solid lines) and experimental data (empty symbols) in Figure 2.2 A shows good agreement. The SRYL model is then used to estimate

the detailed drainage behavior for the pH 10 case in Figure 2.2 B. At time (a) t = 0.5 s, the center of the thin film is flattened because of the repulsive EDL forces. As the force increases to its maximum of 20 nN at time (b) t = 0.6 s, the water film approaches its minimum thickness, which is calculated to be 17 nm on the basis of the balance of surface forces and Laplace pressure that stabilizes the thin film and prevents it from rupturing. The molybdenite surface is then driven away from the dodecane droplet to its original position. The size of the flattened central region of the oil droplet is gradually diminished but maintains its constant thickness at (c) t = 0.9 s and finally departs from the surface at (d) t = 1.05 s just before the interaction force reaches its minimum.

To determine which surface forces are important for the stabilization of the thin water film between dodecane and molybdenite surfaces, individual components of the disjoining pressure were calculated using Equation (2.3), Equation (2.4), and Equation (2.5), as shown in Figure 2.2 C. On the basis of the Hamaker constant for the dodecane/water system ($A_{dwd} = 0.44 \times 10^{-20}$ J) and the molybdenite/water system ($A_{mwm} = 1.8 \times 10^{-20}$ J), the Hamaker constant for molybdenite interacting with dodecane across water in an electrolyte solution (A_{mwm}) was determined to be 0.89×10^{-20} J.[59] According to the contact angle on the molybdenite basal surface of 137° and the dodecane/water interfacial tension of 45 mN/m, the term $\sigma(1 - \cos\theta)$ for the calculation of HB force in Equation (2.5) was determined to be 0.0078 N/m. These two positive terms mean that vdW and HB interactions between dodecane and molybdenite in water appear to be attractive at any separation under experimental conditions of 10 mM NaCl at pH 10. Conversely, it has been confirmed that both the oil droplet and molybdenite surfaces are negatively charged at pH 10.[37] According to the ζ potential of the oil/water interface determined via ζ potential measurement, -60 ± 8 mV , the surface potentials of the oil/water and water/molybdenite

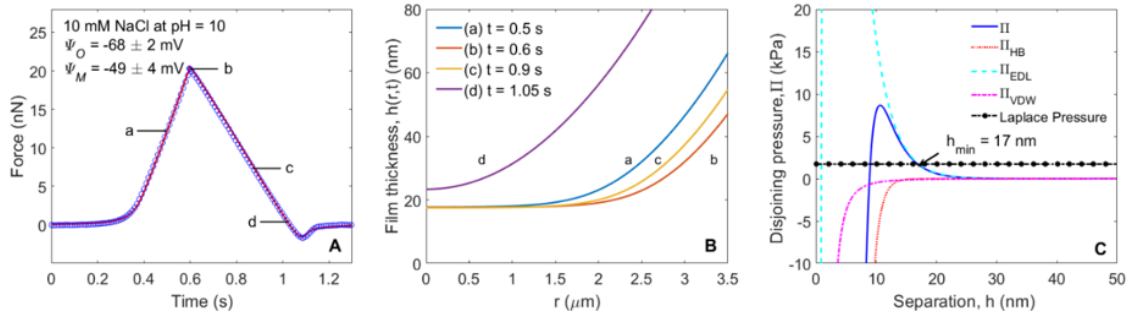

Figure 2.2: Interaction between a dodecane droplet and the molybdenite basal surface in 10 mM NaCl at pH 10 with a driving velocity of 1 μm/s. (A) Empty symbols refer to the experimental force curve during approach and retraction, and the solid line is a theoretical calculation based on the SRYL model. (B) Calculated film thickness at four selected times corresponding to points marked a to d in panel A. (C) Calculated disjoining pressure for this system.

interfaces were -60 ± 8 mV (Ψ_O) and -49 ± 4 mV (Ψ_M) in the SRYL model, which were consistent with literature values.[37, 59] Hence, under these experimental conditions, the EDL force is strongly repulsive. As shown in Figure 2.2 C, EDL forces are the main contributor to the disjoining pressure at separations of $\gtrsim 10nm$. The double-layer repulsion balances the Laplace pressure, $\frac{2\sigma}{R}$, inside the oil droplet at a separation distance of 17 nm, inhibiting further thinning of the intervening film prior to the range of attractive vdW and hydrophobic interaction. Note that in some cases theoretical values for surface potential can be changed by several millivolts without affecting the comparison between experiments and theory.

Force curves obtained for pH values of 4, 6, and 8 in 10 mM NaCl (Figure 2.3) show dramatically different behavior. At each pH, a slight repulsion followed by an instantaneous termination of the deflection signal was observed. The arrow indicates the point when the gradient of the attractive force between the oil droplet and molybdenite exceeds the spring constant of the cantilever. This results in a mechanical instability and further leads to the attachment of the oil droplet to molybdenite. This is termed "jump-in" behavior. The oil droplet detached from the cantilever and jumped onto the molybdenite

when the applied force reached $\sim$ 2.5 nN at pH 4 and $\sim$ 5.5 nN at pH 6, while the "jump-in" behavior was observed with an increased applied force of 9 nN during retraction at pH 8. The significant difference in the force curve measured in 10 mM NaCl at pH 8 can be explained by the calculation of the disjoining pressure from Figure 2.4 B. Compared to the result at pH 10, the repulsive EDL force was weaker. Although the overall disjoining pressure is nearly equal to the Laplace pressure, the attractive hydrophobic force was enough to induce oil attachment. Evolution of the thin water film profile was predicted by the SRYL model and is shown in Figure 2.4 A and at corresponding time points in Figure 2.3 C.

To understand the critical role of pH in the "jump-in" behavior, modeling of the interaction forces was performed extensively at pH 4, 6, and 8 in 10 mM NaCl. At these pH values, the range of EDL forces remained constant due to a constant Debye length of 3.04 nm but the magnitude of EDL forces decreased considerably compared to that at pH 10. We accept that the spontaneous charging of the oil/water interface is attributed to the increasing adsorption of hydroxyl ions that originated from water molecules with an increase in pH.[60] Therefore, reducing the aqueous pH decreased the value of the surface potentials of both the oil droplet and the molybdenite basal plane, which led

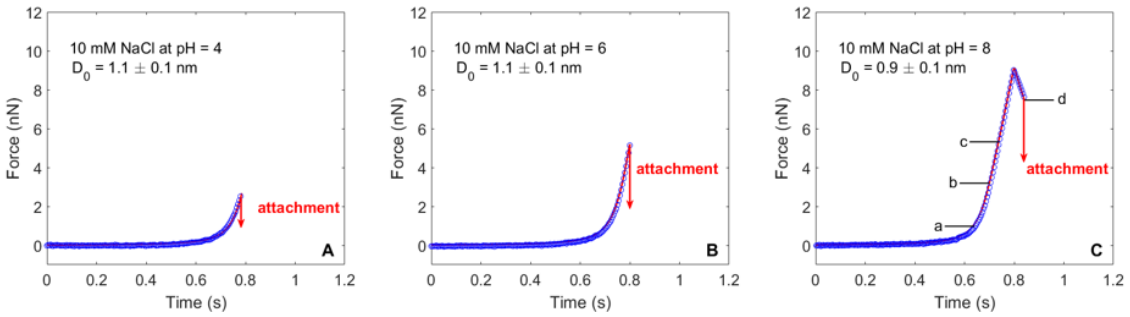

Figure 2.3: Interaction force vs time between dodecane and the molybdenite basal surface in the 10 mM NaCl solution at a driven velocity of 1 μ m/s at (A) pH 4, (B) pH 6, and (C) pH 8. The confined film profile at selected times in panel C is shown in Figure 2.4A.

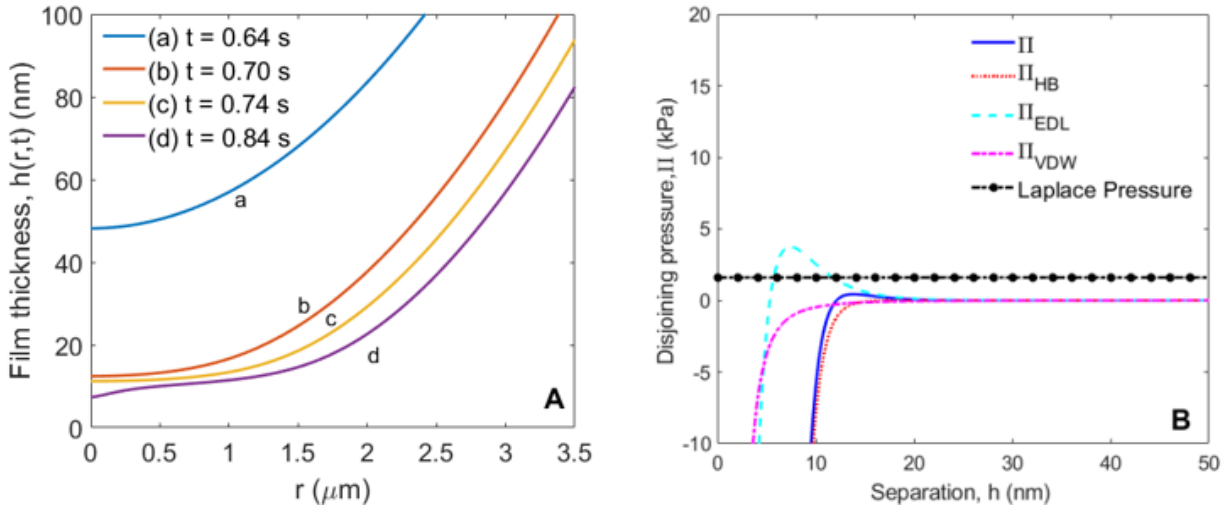

Figure 2.4: (A) Calculated profile of film thickness at four different times corresponding to points in Figure 2.3A. (B) Different components of associated disjoining pressure against separation for the case of pH 8.

to much less electrostatic repulsion. While the vdW component remained unchanged, less EDL repulsion resulted in the attractive hydrophobic force becoming predominant. The overall disjoining pressure was insufficient to stabilize the thin film. As the contact angle is independent of pH, the decay lengths of hydrophobic interaction were therefore determined with the model to be 1.1 ± 0.1, 1.1 ± 0.1, and 0.9 ± 0.1 nm for pH 4, 6, and 8, respectively. The thin water film kept draining and ruptured at the point "jump-in" behavior occurred. The critical film thicknesses were calculated to be < 10 nm for pH < 8. Oil droplet deformation showed a trend similar to that in Figure 2.2 B. during the approach [from time (a) to time (c)] but exhibited an instantaneous "pimple" before attaching onto molybdenite at time (d) t = 0.84 s as shown in curve d of Figure 2.4 A.

2.3.2 Effects of the electrolyte on the interaction between oil and molybdenite

Similar experiments were carried out to evaluate the effects of salt concentration on the surface forces between a dodecane droplet and molybdenite basal plane. Figure 2.5 A

represents the interaction forces between a dodecane oil droplet and molybdenite basal plane as the two surfaces were brought into the proximity of each other in 100 mM NaCl at pH 10. "Jump-in" behavior was observed with an applied force of $\sim$ 2.2 nN indicating that the dodecane oil droplet pulled the cantilever down and the droplet spread over the molybdenite basal plane. Good agreement between theory and experimental data in Figure 2.5 A was obtained when the decay length of hydrophobic interaction was 1.2 ± 0.1 nm. Inspection of Figure 2.5 B showed that with negligible hydrodynamic effects, a pimple occurred before rupture at time (d) t = 0.810 s. The components of disjoining pressure were calculated as a function of dodecane-molybdenite separation using Equation (2.3), Equation (2.4), and Equation (2.5) as shown in Figure 2.5 C. The vdW component in this interaction remained the same as for 10 mM NaCl and attractive for the specific oil. When the Debye length of electrostatic interaction of 0.96 nm for 100 mM NaCl is taken into account, the EDL repulsion is significantly suppressed relative to that with 10 mM NaCl at pH 10. The hydrophobic interaction became the primary component and mostly coincided with the overall disjoining pressure as shown in Figure 2.5 C. The critical central separation (h_{min}) is shorter for 100 mM NaCl, which was calculated to be $\sim$ 10 nm by comparison with the value of 17 nm for a 10 mM NaCl solution at pH 10. This reveals that a higher salinity weakens the EDL repulsion and facilitates the attachment of the oil to the molybdenite surface.

Calcium oxide is usually used in the flotation circuit to achieve selective flotation of molybdenite and chalcopyrite at alkaline pH. Understanding the role of Ca^{2+} in the floatability of molybdenite is therefore particularly important. Lucay et al. [56] reported the undesirable effect of calcium ions in the presence of sulfate ions. The detrimental results of Ca^{2+} on molybdenite recovery have also been reported by Hirajima et al. [61]

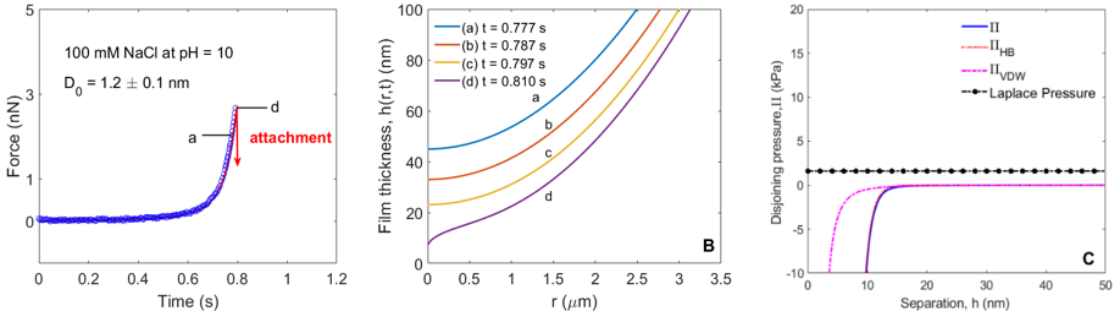

Figure 2.5: (A) Interaction force vs time between dodecane and molybdenite basal surface in a 100 mM NaCl solution at a driven velocity of 1 μm/s at pH 10. (B) Calculated profile of film thickness at four different times corresponding to points in Figure 2.5 A. (C) Different components of associated disjoining pressure vs separation.

at pH > 9. One argument in favor of Ca^{2+} on the molybdenite flotation is the fact that the adsorbed Ca^{2+} ions decrease the magnitude of the surface potentials of molybdenite and bubbles at high pH and further weaken the EDL repulsion between them.[62] In the work presented here, AFM experiments were carried out in a 3.3 mM $CaCl_2$ solution at pH 10 to retain the same ionic strength of sodium ions (10 mM) and remove the influence of precipitates. Repulsion was also observed from the interaction forces between oil droplet and molybdenite basal plane, as shown in Figure 2.6 A. Using the ζ potentials of oil of $-23 \pm 5mV$ from the ζ potential measurement, the surface potentials of oil and molybdenite were determined to be $-25 \pm 5mV$ and $-23 \pm 3mV$, respectively, from the direct comparison of these experimental data to the theoretical calculations. This indicates that the presence of Ca^{2+} resulted in less negative surface potentials of oil/water and molybdenite/water interfaces as compared to the respective surface potentials for NaCl solutions ($\Psi_{O,NaCl} = -68 \pm 2mV$ and $\Psi_{M,NaCl} = -49 \pm 4mV$). This agrees well with the previous findings by Raghavan,[62] who proposed that the adsorbed calcium ions on molybdenite can increase the ζ potential of molybdenite. Figure 2.6 B reveals that the thin water film between oil droplets and molybdenite evolved in a manner similar to that seen in 10 mM NaCl at pH 10, where it stopped draining after reaching the equilibrium

thickness of 14 nm at time (b) t = 0.6 s. The corresponding disjoining pressure calculations are shown in Figure 2.6 C. In comparison with Figure 2.2 C, the effect of Ca^{2+} became significant, less negative surface potentials allowing the EDL repulsion to weaken, and the thinner water film, while the EDL repulsion still exceeded the Laplace pressure and prevented attachment. More interaction force measurements in the $CaCl_2$ solution were conducted and are described in the next section in an effort to understand the role of Ca^{2+} in the interaction between the oil droplet and molybdenite basal plane.

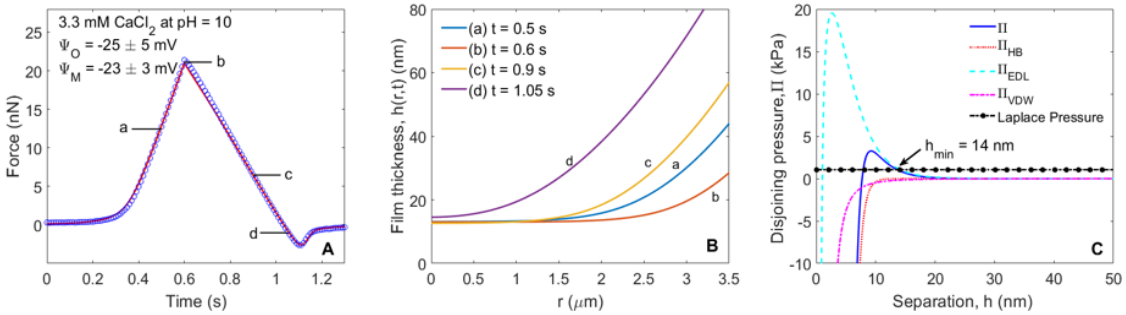

Figure 2.6: (A) Interaction force vs time between dodecane and the molybdenite basal surface in a 3.3 mM $CaCl_2$ solution at pH 10 at a driven velocity of 1 μm/s. (B) Calculated profile of film thickness at four different times corresponding to the points in Figure 2.6 A. (C) Different components of associated disjoining pressure vs separation.

2.3.3 Stability map of the interaction between oil droplets and molybdenite

Stability maps are commonly used in the literature to indicate regions where interactions are repulsive or attractive to result in attachment and/or coalescence. For example, a stability map showing the critical force required for coalescence was presented for micrometer-sized bubble-bubble or drop-drop interaction based on the knowledge obtained from the experiment and the SRYL model.[63, 64] For our study, the attachment or non-attachment outcomes of force measurements are summarized in the stability map shown in Figure 2.7. We note that no experiments were performed in the $CaCl_2$ solution above pH 11 to rule out the possible effect of $CaCO_3$ or $Ca(OH)_2$ precipitate. The attachment region

denotes cases in which the thin water film between dodecane droplets and molybdenite surfaces ruptured and the dodecane droplet jumped into the molybdenite basal plane during either the approach or the retraction process. The non-attachment region represents cases in which the interaction was stable. The dodecane droplet probe was driven toward the molybdenite up to an interaction force of 20 nN and retracted without any loss of dodecane; the water film reached a minimum thickness without rupture. By drawing a line between attachment (empty symbols) and nonattachment (filled symbols) experimental points for NaCl, we separated the different regions. Similarly, the non-attachment region for the $CaCl_2$ solution was smaller as indicated in Figure 2.7. Conversely, the gray region that favors attachment in the NaCl solution is smaller than that of the $CaCl_2$ solution. This discrepancy between the two regions suggests that calcium ions are beneficial for the attachment of oil to the molybdenite basal plane when compared to sodium ions at the same ionic strength. The underlying reason can be explained by the adsorbed $Ca(OH)^+$ on the molybdenite basal plane that makes the surface potentials less negative, decreases the magnitude of EDL repulsion, and possibly reverses the surface potentials at high concentrations.[65] This result also implies that the interaction between oil and the molybdenite basal plane in the presence of $CaCl_2$ is not directly responsible for the depression of molybdenite floatability at alkane pH when the ionic strength is > 10 mM.[66, 67]

From previous analysis and discussion, in the non-attachment regions, the EDL repulsion is greater than the Laplace pressure and the dominant force governing dodecane-molybdenite interaction. For the attachment regions, the repulsive EDL force is decreased and the attractive HB force dominates, resulting in the "jump-in" behavior and unstable interactions. In addition, stable interactions were observed at pH 7 in a 0.1 mM NaCl

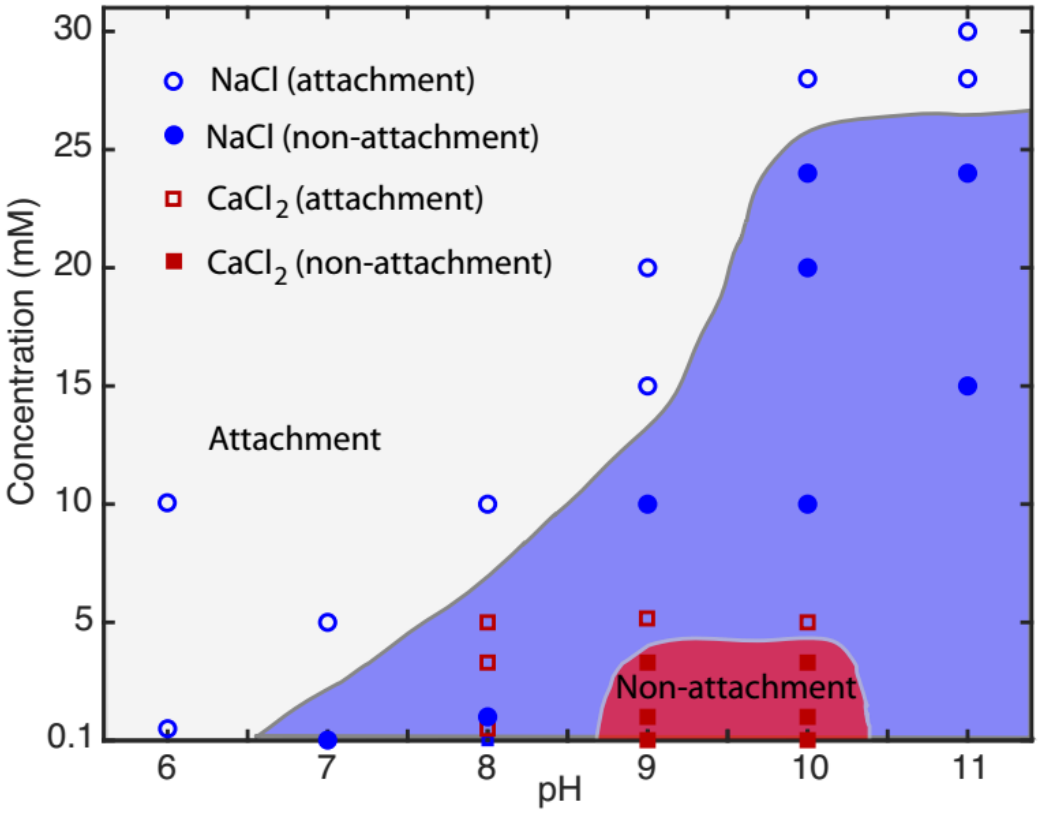

Figure 2.7: Stability map of the interaction between dodecane and the molybdenite basal surface in an electrolyte solution for varying salt concentrations, salt types, and pH values. The red and blue regions represent non-attachment behavior in $CaCl_2$ and NaCl solutions, respectively, while the gray region indicates where attachment happens.

solution and then at pH 8 in a 0.5 mM NaCl solution, with a gradual increase in salt concentration and pH value until pH 10 and 11 in a 24 mM NaCl solution. In contrast, the non-attachment region for the $CaCl_2$ solution shows a different trend, where stable interactions occur only between pH 9 and 10 below a $CaCl_2$ concentration of 3.3 mM, namely, an ionic strength of 10 mM. The stability map from our experimental results provides a direct comparison of the effects of sodium and calcium ions on the interaction between dodecane and the molybdenite basal surface and prediction of the behavior of yet unexplored conditions.

2.3.4 Zeta potential of dodecane

ζ potential of dodecane droplets were measured as reference value for theoretical calculation shown in Figure 2.8

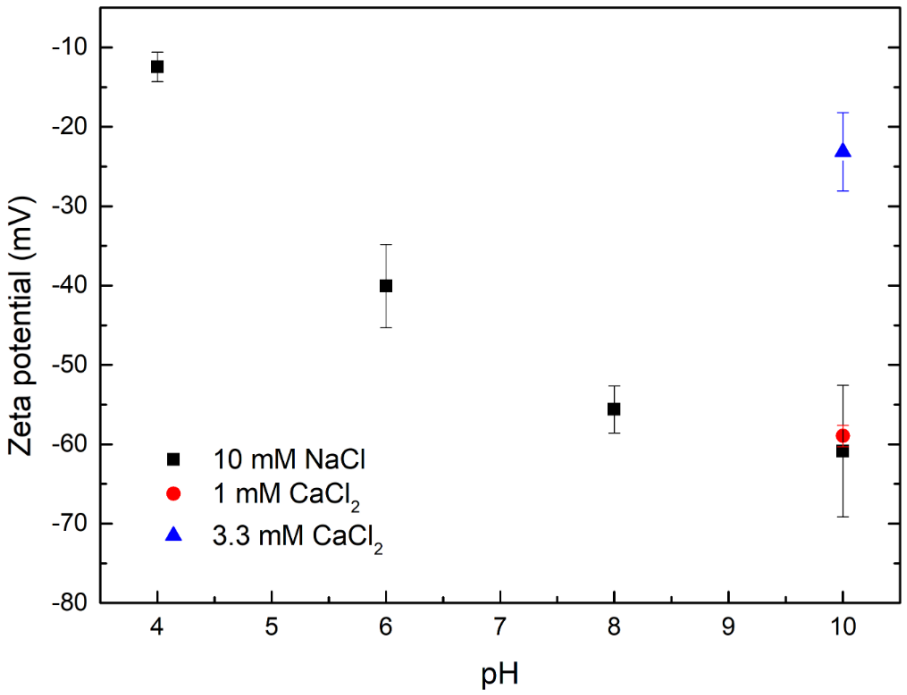

Figure 2.8: Measured zeta potential of dodecane droplets as a function of pH in 10 mM NaCl (black square), 1 mM $CaCl_2$ (red circle), and 3.3 mM $CaCl_2$ (blue triangle).

2.3.5 Dodecane/water interfacial tension

Dodecane/water interfacial tension was measured to confirm the absence of surface-active components (Table 2.1).

Table 2.1: The interfacial tension of dodecane/water interface under different conditions.

Aqueous condition	Interfacial tension (mM/m)
Milli Q water	45.4 ± 0.7
10 mM NaCl at pH 4	44.6 ± 0.6
10 mM NaCl at pH 10	44.4 ± 0.6
10 mM $CaCl_2$ at pH 8	45.1 ± 0.9

2.3.6 Contact angle of dodecane on molybdenite basal plane

An image of dodecane drop is shown in Figure 2.9 and measured contact angles at different pH are given in Figure 2.10 .

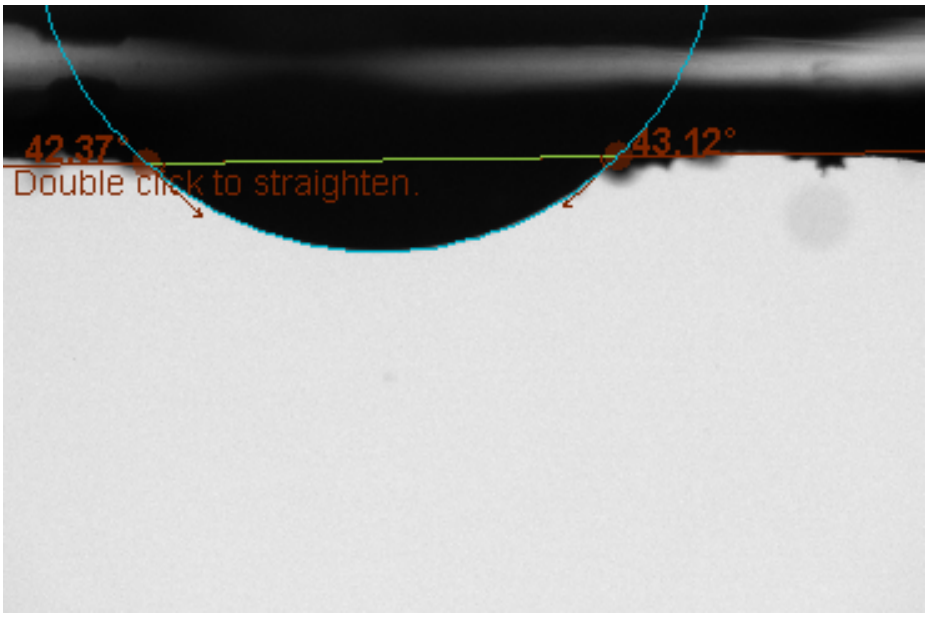

Figure 2.9: Image of a dodecane drop on molybdenite basal plane obtained in 10 mM NaCl at pH 8.

2.3.7 Induction timer

Induction timer experiments were performed to further confirm the AFM results. Table 2.2 shows a sharp decrease in induction time required for bubble attachment onto molybdenite basal plane after oil coating (5750 ms for bubble/MoS_2 to 50 ms for bubble/oil-coated MoS_2). Additionally, the induction time for oil droplet attachment onto the bare molybdenite basal plane under attachment condition was shorter than the one under non-attachment condition obtained from the paper (150 ms vs. 1200 ms). The results of induction timer are consistent with the data reported in the manuscript.

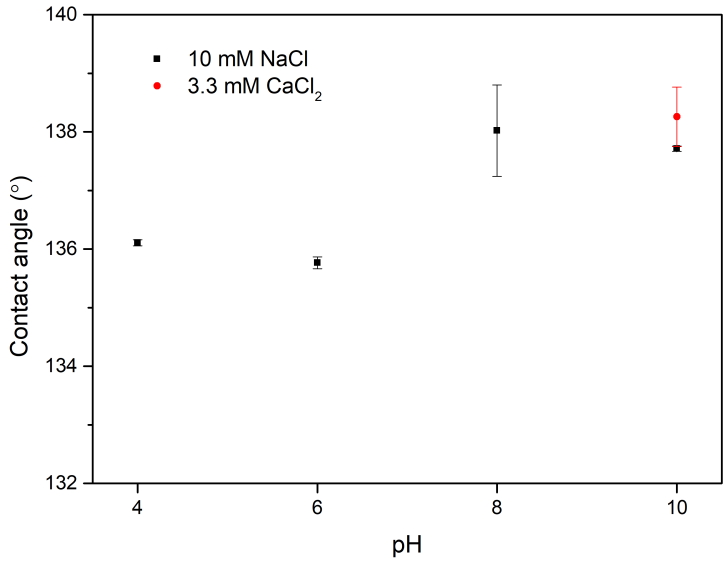

Figure 2.10: Contact angles of dodecane on molybdenite basal plane obtained at different pHs.

Table 2.2: Experimental results using induction timer to compare with the AFM data.

	Bubble – MoS_2 (0.5 mM NaCl pH 10)	Bubble – oil coated MoS_2 (0.5 mM NaCl pH 10)
Time (ms)	5750	50
	Oil – MoS_2 (0.5 mM NaCl pH 10) (non–attachment condition for AFM)	Oil – MoS_2 (30 mM NaCl pH 4) (attachment condition for AFM)
Time (ms)	1200	150

2.3.8 Comparison of constant charge and constant potential model

Constant surface potential boundary condition was assumed and applied for all theoretical calculation. Here constant surface charge boundary condition is considered to compare and evaluate the possible difference between two conditions. The interaction force between dodecane and molybdenite basal plane in 3.3 mM $CaCl_2$ at pH 10 was reevaluated by constant charge boundary condition as shown in Figure 2.11. Disjoining pressure of electrical double layer (EDL) by assuming constant surface charge boundary condition:[68]

$$\Pi_{EDL}(h) = \frac{2\Psi_0^2 + \Psi_0\Psi_M\left(e^{\kappa h} + e^{-\kappa h}\right) + \Psi_M^2}{\varepsilon_0\varepsilon\left(e^{\kappa h} - e^{-\kappa h}\right)^2} \tag{2.8}$$

From Figure 2.11 A, the interaction force still agrees well with the theoretical calculation where disjoining pressure of EDL is calculated under constant surface charge boundary condition. Figure 2.11 B compares disjoining pressure of EDL under constant surface charge and constant surface potential boundary conditions. Two curves intersect the Laplace pressure at one point. In addition, the corresponding total disjoining pressure exhibited the same magnitude and exceeded the Laplace pressure at separation $h = 14nm$ (Figure 2.11 C). Therefore, it is reasonable to say that constant surface charge boundary conditions can also be assumed for the calculation of interaction force between dodecane and molybdenite basal plane.

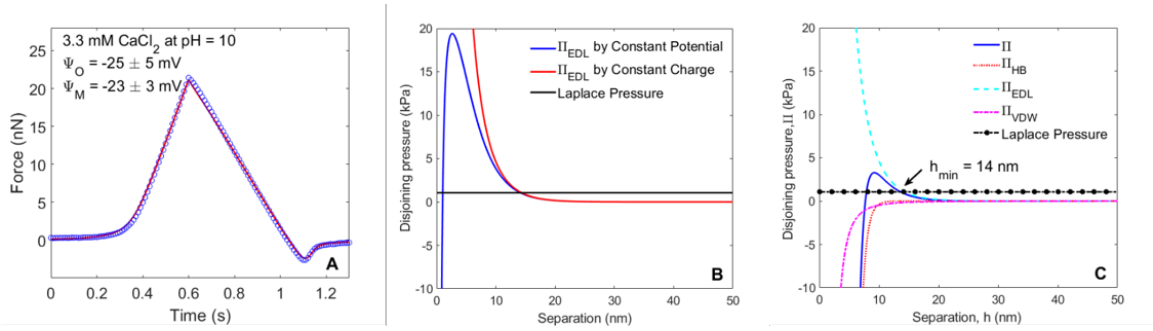

Figure 2.11: (A) Interaction force versus time between dodecane and molybdenite basal surface in 3.3 mM $CaCl_2$ solution at a driven velocity of 1 µm/s at pH 10. (B) Disjoining pressure of EDL under constant surface charge (CC, red line) and constant surface potential (CP, blue line) boundary conditions. (C) Different components of associated disjoining pressure against separation.

2.3.9 Interaction force between molybdenite basal plane and dodecane

AFM force curves for cases not shown in the manuscript are given in Figure 2.12 and Figure 2.13.

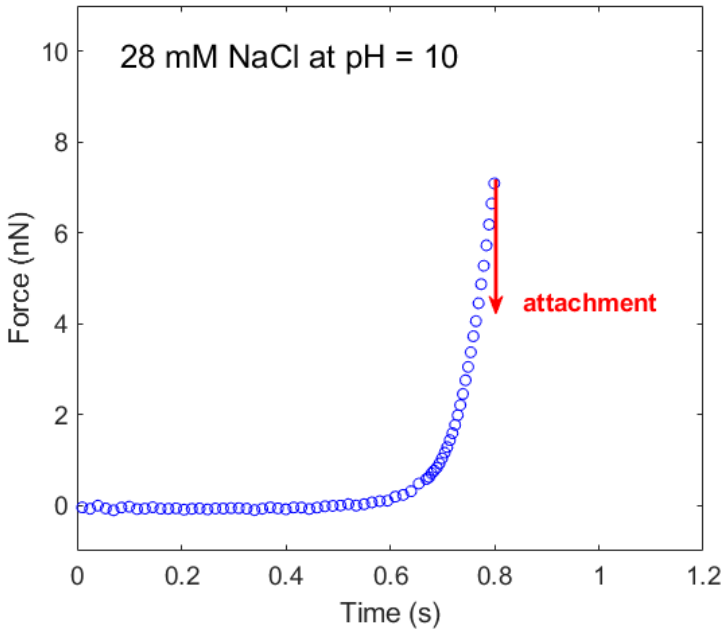

Figure 2.12: Interaction force versus time between dodecane and molybdenite basal surface in 28 mM NaCl solution at a driven velocity of 1 μm/s at pH 10.

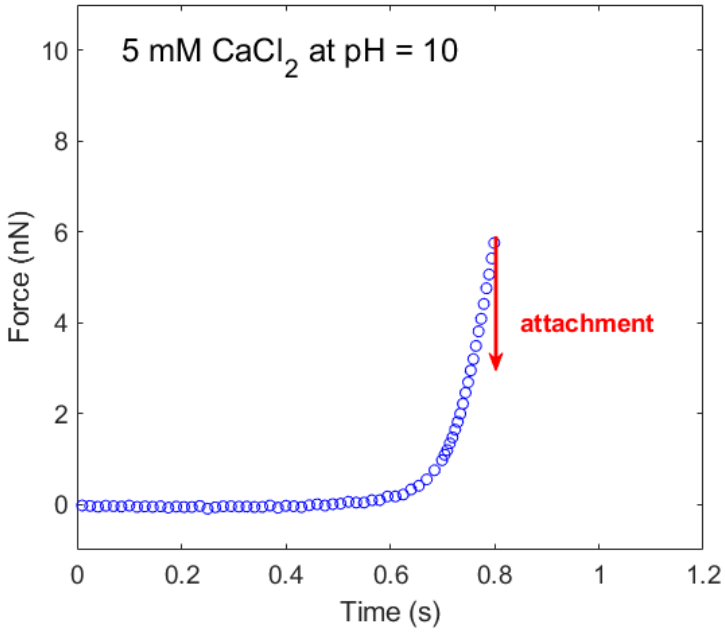

Figure 2.13: Interaction force versus time between dodecane and molybdenite basal surface in 5 mM $CaCl_2$ solution at a driven velocity of 1 μm/s at pH 10.

2.4 Summary and conclusions

In this study, we investigated the mechanisms of interaction between nonpolar oil and molybdenite using dodecane as a model oil. Direct force measurement performed by the AFM droplet probe technique provided quantitative information about the intermolecular forces between a dodecane oil droplet and molybdenite mineral basal plane. The Stokes-Reynolds-Young-Laplace model was compared with experimental data obtained under various aqueous conditions and provided insight into the impact of vdW, EDL, and HB forces for each experimental condition. At high pH and low salinity, both the oil droplet and the molybdenite surface were strongly negatively charged, arising from the adsorption of hydroxyl ions originating from the water. Under these conditions, strong EDL repulsion dominated and no oil attachment was observed. By contrast, low pH and high salinity are conducive to the attachment of oil to molybdenite due to a suppression of surface potential and Debye length, respectively, which both reduced repulsive EDL forces. From the stability map, Ca^{2+} exerted a stronger effect on the attachment behavior between the oil droplet and molybdenite basal plane than Na^{+} at the same ionic strength. The methodology employed here consisted of both a precise experimental protocol and a reasonable theoretical explanation that provided a valuable proof of concept. The ability to characterize surface forces, estimate surface potential, and predict the best condition for the floatability of molybdenite for various aqueous chemistries and hydrophobic additives will continue to be highly beneficial to the field of mineral chemistry.

Chapter 3

Understanding Wettability of Millerite by Using Atomic Force Microscopy

3.1 Introduction

Millerite is a needle-like nickel sulfide with rhombohedral crystal form (β-NiS). It is usually associated with chalcopyrite ($CuFeS_2$) and pentlandite $(Fe, Ni)_9S_8$. The separation of copper and nickel has been viewed as a critical step for copper bearing ore. Recently, millerite was found to be responsible for the high nickel concentration in the Sudbury basin. However, the nickel grade in copper concentrate is generally expected to be lower than 0.6% to meet the quality specification.[69] Millerite is more floatable than other nickel sulfides, such as pentlandite. Conventional depressing practice for nickel sulfide, such as the addition of sodium cyanide or high-lime aeration conditioning yield insufficient depression of millerite.

Considerable effort has been made to understand the impact of water chemistry on millerite flotation. Like other sulfide minerals, millerite is extremely sensitive to aqueous condition where oxidation can easily happen and ultimately influence flotation recovery. Xiong et al. [70] has studied oxygen adsorption on the (001) surface of millerite by Ab Initio density functional studies. Their work has shown that parallel adsorption is more stable than vertical adsorption and oxygen may easily experience dissociation on millerite surface. X-ray photoelectron spectroscopy (XPS) also provided information on reaction product after air and water oxidation.[71] It was observed that polysulfide (S_n^{2-}) and nickel hydroxide ($Ni(OH)_2$) species formed on water-reacted millerite while nickel sulfate ($NiSO_4$) and nickel hydroxide ($Ni(OH)_2$) found on air-oxidized sample. Better understanding of surface properties of millerite under different water chemistry is of fundamental and practical importance to developing a possible pathway of separation of copper and nickel. As an indispensable tool, Atomic Force Microscopy (AFM) has been widely applied in mineral flotation, where direct force measurement has shown the surface

potential of minerals[59], topographic image has elucidated the butyl xanthate adsorption on galena,[72] and the bubble probe technique has provided fundamental information on bubble-particle interactions that are involved in flotation. [24, 51]

In this paper, surface potential and wettability of millerite in 10 mM KCl at pH 4 and pH 12 were studied through direct measurements of the bubble-mineral interactions by the AFM bubble probe technique. With further theoretical modelling, the surface forces for the bubble-millerite system were revealed and quantitatively analyzed. This fundamental study was designed to understand the millerite surface properties and provide useful information for millerite depression.

3.2 Experimental section

3.2.1 Materials and mineral sample preparation

Naturally formed millerite (β-NiS) originated from Sudbury, Ontario of Canada was purchased from kaygeedee Minerals. Examination by X-ray fluorescence (XRF) and X-ray powder diffraction (XRD) analysis were conducted and showed 96% purity with minor chalcopyrite. Potassium chloride (KCl), sodium hydroxide (NaOH, 1N), and hydrochloric acid (HCl, 1N) at ACS reagent grade purchased from Fisher Scientific were used to prepare 10 mM KCl solution at pH 4 and pH 12. A fresh cleavage piece of millerite was glued with epoxy on a glass slide. Prior to AFM force measurement, this millerite sample was ultrasonicated for 5 min, rinsed with Milli-Q water and gently dried under nitrogen stream. The millerite was then placed in the target solution for 30 minutes to reach equilibrium.

3.2.2 Force measurement

The interaction forces between bubble and millerite were measured by an MFP-3D AFM system (Asylum Research, Santa Barbara) mounted on a Carl Zeiss Observer A1 inverted microscope. The bubble probe technique is shown in Figure 3.1. A custom-fabricated rectangular AFM cantilevers ($450 \times 50 \times 2\mu m^3$) with gold patch on the end was first hydrophobized by 10 mM 1-dodecanethiol ethanolic solution, it was then used to pick up an air bubble with radius 50∼60 μm. Micron-size bubble was generated by an ultra sharp pipette. Photodiode voltage versus linear variable differential transformer (LVDT) was first tracked as raw data and then calculated to force-time data by multiplying by spring constant of the cantilever, which was determined to be 0.2∼0.3 N/m. To ensure reproducibility, at least five bubbles were tested at different spots on millerite surface for each condition.

3.2.3 Theoretical modelling

A well-established theory, known as the Stokes-Reynolds-Young-Laplace (SRYL) model, was employed to quantitatively model the interaction force between the bubble and millerite. SRYL model constitutes of two equations: (1) the Stokes-Reynolds equation Equation (3.1) modelling the evolution of the thin film drainage process:

$$\frac{\partial h}{\partial t} = \frac{1}{12\mu r}\frac{\partial}{\partial r}\left(rh^3\frac{\partial p}{\partial r}\right) \tag{3.1}$$

where h is the water film thickness, r is the radial coordinate, μ is the viscosity of the aqueous solution, and p is the hydrodynamic pressure in the thin film between the bubble and surface. An immobile boundary condition was assumed at both the air-water and air-molybdenite interfaces.[55]

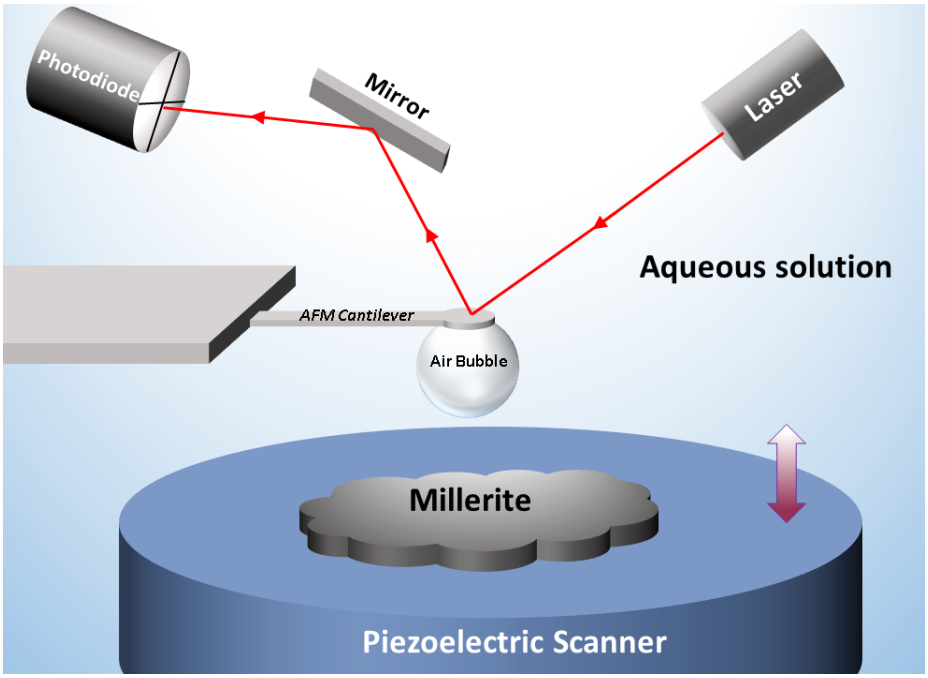

Figure 3.1: Diagram depicting the typical AFM bubble probe technique

(2) The Young Laplace equation Equation (3.2) for the mathematical description of bubble deformation arising from the disjoining pressure Π and hydrodynamic pressure:

$$\frac{\sigma}{2r}\frac{\partial}{\partial r}\left(r\frac{\partial h}{\partial r}\right) = \frac{2\sigma}{R} - \Pi - p \tag{3.2}$$

where σ is the air/water interfacial tension, and R is the radius of the bubble, and Π is the overal disjoining pressure. For bubble-millerite interaction in 10 mM KCl, three surface forces should be accounted for: van der Waals (vdW) force, electrical double layer (EDL) force, and hydrophobic (HB) force. An expression for the overall disjoining pressure is then obtained:

$$\Pi = \Pi_{vdW} + \Pi_{EDL} + \Pi_{HB} \tag{3.3}$$

For the sake of brevity, four boundary conditions for SRYL model and detailed calculations for three surface forces can be found in section 3.2.4. [73]

3.3 Results and discussion

Force measurements between an air bubble and millerite in 10 mM KCl at pH 4 are shown in Figure 3.2 A. The open symbols show representative experimental data and solid line is the theoretical calculation based on the SRYL model. At pH 4, the force curve was slightly repulsive followed by a sudden termination when the applied force just exceeded 3 nN. This behavior was referred as "jump-in".[74] The bubble pulled down the cantilever, attached onto millerite surface immediately after contact and spread over. The positive Hamaker constant for interaction of air bubble and millerite across water implies that vdW force is repulsive.[75] The SRYL model describing vdW, EDL, and HB forces was then fitted to the experimental data to estimate the surface potential of bubble and millerite and the magnitude of attractive hydrophobic force. In our previous work, the zeta potential of millerite particles was found to be around -39 ± 4 mV at pH 4. The surface potential of bubble and millerite were then estimated as -30 ± 3 mV and -35 ± 4 mV , respectively.[76] Both vdW and EDL forces are responsible for the repulsion observed in the force curve. Hydrophobicity of millerite at pH 4 was confirmed by contact angle measurement where the contact angle was seen to be 60°. The term $\sigma(1 - \cos\theta)$ for the calculation of the HB force in Equation (2.5) was then determined to be 0.036 N/m. A decay length of 1.5 ± 0.1 nm was derived to well describe the range of the hydrophobic attraction. The disjoining pressure has been calculated according to these parameters and is shown in Figure 3.2 B. The hydrophobic force shows longer range and is stronger than the EDL repulsion and thus the bubble jumps into the surface at a critical film thickness around 12.5 nm.

Previous XPS studies and ICP solution species analysis suggested that elemental sulfur and/or polysulfide (S_n^{2-}) formed from an amount of released nickel ions under acidic conditions.[77] This species is strongly hydrophobic and thus can explain the negative

charge and hydrophobicity of millerite at pH 4. Additionally, the dissociation of nickel ion lead to nano-roughness in the contact area. Given the discussion above, bubble attachment onto millerite surface can be easily induced at pH 4.

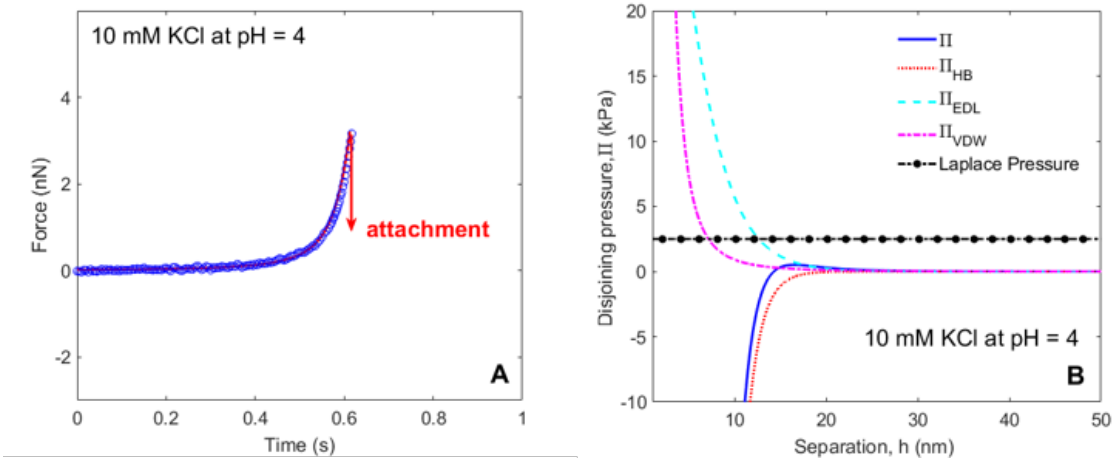

Figure 3.2: Measured forces between bubble and millerite in 10 mM KCl at pH 4 with a driving velocity of 1 μm/s. (A) Open symbols are experimental AFM data and solid line is the theoretical fit using the SRYL model. (B) Calculated disjoining pressure for this system.

In the case of 10 mM KCl at pH 12, the behavior of the interaction was considerably altered: the force curve was repulsive when applied force reached 5 nN, and upon retraction the bubble returned back to its original position without jump-in (Figure 3.3 A). It is important to note that a strong adhesive pull appeared during retraction which implies the bubble had contacted with millerite surface but managed to detach from the surface with a pull-off force of 2 nN. The three phase contact line did not expand during contact. A discrepancy between theoretical fit and experimental data is presented. A possible reason for this could be the limitation of the theory. Whilst SRYL model describes well the bubble deformation against a smooth surface, it assumes perfectly smooth surfaces and does not take bubble adhesion into consideration. In other words, calculation regarding the bubble deformation stops where bubble attachment happens.

Concerning the influence of alkaline condition on bubble-millerite interaction, contact

angle measurement, zeta potential and XPS were also conducted for surface characterization.[77] Compared to pH 4, contact angle of millerite decreased to 43° in 10 mM KCl at pH 12 indicating less hydrophobicity of millerite. The released nickel ions were oxidized by dissolved gas and formed hydrophobic polysulfide [78]. The formation of hydrophilic $Ni(OH)_2$ was also found by XPS analysis. The precipitate acted as a passivation layer and prevented the formation of more polysulfide. The mixture of polysulfide and nickel hydroxide allowed for the partial hydrophobicity of millerite at pH 12. By using this information, contributions of each force were determined: while vdW stayed repulsive at small separation, HB attraction decreased, and EDL respulsion increased and dominated over HB force. Millerite surface potential remained -33 ± 4 mV which was consistent with zeta potential of -30 ± 6 mV. Bubble showed more negative charge (-63 ± 4 mV) as a result of more OH^- adsorbing at the air-water interface at pH 12. [79] As given in the corresponding disjoining pressure calculation (Figure 3.3 B), the thin water film stopped draining when the thickness reached 14.6 nm due to the EDL repulsion.

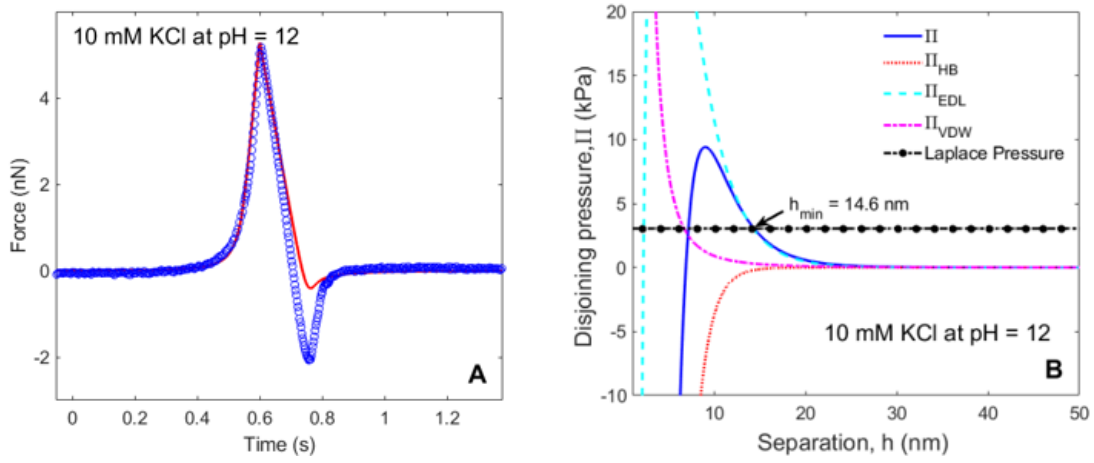

Figure 3.3: Measured forces between bubble and millerite in 10 mM KCl at pH 12 with a driving velocity of 1 μm/s. (A) Open symbols are experimental AFM data and solid line is the theoretical fit using the SRYL model. (B) Calculated disjoining pressure for this system.

3.4 Conclusion

The wettability and surface potential of millerite under pH 4 and pH 12 were investigated using the AFM bubble probe technique. Experimental data suggested that acidic condition favors bubble-millerite attachment while reaction production from pH 12 impart millerite surface less hydrophobic than in pH 4. Apart from AFM force measurement, the SRYL model was employed and exhibited good agreement with experimental results. This has led to an extensive understanding in terms of surface forces.

Chapter 4

AFM studies of pentlandite oxidation induced by H_2O_2

4.1 Introduction

Pentlandite (Pn, $(Fe, Ni)_9S_8$) is the main nickel-producing constituent of nickel sulphide ore. Generally, pentlandite can be recovered through flotation with the addition of thiol collectors at pH 9. The common association of pentlandite, pyrrhotite (Po, $Fe_{1-x}S$), is typically considered as gangue mineral and its rejection is desired due to the difficulties in removing sulfur in it. Similarities between pentlandite and pyrrhotite represented significant challenge in separating the two minerals. Therefore it is cricial to understand the surface properties of pentlandite.

There has been no consensus on the role of oxidation in the selectivity of Pn and Po. In 2005, Legrand et al. [80] proposed that low O_2 concentrations in pulp solutions was able to facilitate the separation of Po from Pn. X-ray photoelectron spectroscopy (XPS) results suggested that the major oxidation products on Pn and Po surfaces from dissolved oxygen are ferric oxyhydroxide (FeOOH) overlayers. In addition, violarite ($FeNi_2S_4$) and nickel hydroxide $Ni(OH)_2$ can be detected on pentlandite using the same technique. When dissolved O_2 concentrations were as low as 0.03 ppm, the Po surfaces were found to be heavily oxidized, while the Pn surfaces remained relatively unchanged. Meanwhile, it was also found that excessive oxidation of the sulfide mineral potentially leads to reduced recovery of pyrrhotite.[81–84]

In this work, H_2O_2 was chosen to induce the oxidation on pentlandite at pH 9.3. H_2O_2 was chosen for its role as a strong oxidizing agent in alkaline conditions:[85]

$$H_2O_2 + 2H^+ + 2e^- \rightleftharpoons 2H_2O \tag{4.1}$$

The AFM bubble technique was employed to understand the interaction between

pentlandite and a micron-size air bubble. This approach, accompanied by the well-established SRYL model, enabled us to quantitatively understand the bubble attachment behavior. Furthermore, the hydrophobicity of pentlandite surface with or without H_2O_2 conditioning were evaluated by contact angle measurement, AFM topography images, and adhesion force map. This work provides fundamental information on the oxidation of pentlandite by H_2O_2 and provides insight into the possible selective flotation of pyrrhotite from pentlandite.

4.2 Experimental Section

4.2.1 Materials and Sample Preparation

Pure pentlandite specimens were obtained from Vale's Sudbury plant, Ontario of Canada. Milli-Q water with a resistivity of 18.2 $m\Omega \cdot cm$ from a Barnstead Nanopure system (Thermo Fisher Scientific) was used to prepare all aqueous solutions. All glassware was cleaned by being repeatedly rinsed with toluene, acetone, Milli-Q water, and acetone again and then dried with high-purity nitrogen. Hydrogen peroxide solution (H_2O_2, ACS reagent, 30 wt % in H_2O), sodium tetraborate decahydrate ($Na_2B_4O_7$, ACS reagen, 99.5 %), and octadecyltrichlorosilane (OTS, $C_{18}H_{37}Cl_3Si$, 95%) were bought from Sigma and used as received. Potassium isobutyl xanthate (PIBX, $C_5H_9OS_2K$, MW =188.35) was purified by recrystallization from acetone-ether solutions according to an established method.[86]

Pentlandite composition was examined by a Scanning Electron Microscope (SEM) fitted with Energy Disperse X-ray Spectra (EDS). The pentlandite sample was embeded into epoxy resin within a cylinder mold of 5 mm diameter. Prior to each experiment, the mineral surface was carefully polished with wet silicon carbide paper of 600, 800, and 1200 grit, then polished on MicroCloth with 9, 3, 0.05 μm alumina suspension, rinsed by

Milli-Q water, sonicated for 5 min, and dried by nitrogen blow. All the aqueous solutions used in this work were well sealed and purged with nitrogen for at least 30 minutes before any experiments. For H_2O_2 and PIBX conditioning, pentlandite surface was first exposed to 10^{-5} M hydrogen peroxide in 0.05 M borax buffer solution for 3 min, then 10^{-5} M PIBX was added to the solution. After another 3 minutes, the sample was removed from the mixed solution, rinsed by the borax buffer solution, and transferred to the buffer solution. For PIBX condition, the pentlandite surface was immersed in 10^{-5} M PIBX in 0.05 M borax buffer solution for 3 minutes, taken out and rinsed for futher experiments. The exposure time for each solution was strictly controlled within 3 minutes. A magnetic stirring bar was used during conditioning. Special care was taken during the sample transferring to avoid oxidation by air.

4.2.2 Contact angle measurement

The contact angle of a captive bubble on pentlandite after conditioning was measured by a Theta Optical Tensiometer T200 (Biolin Scientific, Stockholm, Sweden) at room temperature. The interafacial tension of the air/water interface in borax buffer solution, 10^{-5} M H_2O_2 borax buffer solution, 10^{-5} M H_2O_2 and 10^{-5} M PIBX borax buffer solution, and 10^{-5} M PIBX borax buffer solution were found to be 71.4 ± 0.8 mN/m by Tensiometer. For the captive bubble method, at least five bubbles at different spots were recorded.

4.2.3 AFM measurement

All AFM force measurements were carried out by applying the method described in 4.2.2. Topography images were obtained by AFM tapping mode in borax buffer solution. Bruker's silicon nitride probes with a spring constant of 0.07 N/m, DNP-10, were used for adhesion force map. Before being used for AFM experiment, Si_3N_4 probes were first

cleaned by UV-ozone and hydrophobized by immersion in 2 mM OTS-toluene solution for 30 min. They were then rinsed by copious amount of toluene and acetone and dried by nitrogen blow. Force map mode from MFP-3D AFM system (Asylum Research, Santa Barbara, CA) was used. Interaction forces between OTS tip and pentlandite were measured consecutively on 20×20 grid points over a 2×2 μm^2 area. The adhesion force map was simultaneously produced by Asylum Research software. The loading force was set to be 2 nN and the approaching velocity was 1 μm/s. The adhesion force was calculated and analyzed by Asylum Research software.

4.2.4 Theory

The extensively validated Stokes-Reynolds-Young-Laplace (SRYL) model was employed to quantitatively analyze the interaction between air bubble and the mineral surface. Detailed explanation for the SRYL model can be found in section 3.2.4 and 4.2.3.

Since all the experiments were performed in buffer solutions (0.05 M sodium borate), with ionic strength of 0.15 M, the Debye length is considerably short. Therefore, electrical double-layer (EDL) can be neglected in this system.[40] When the contact angle is less than 40°, only vdW force contributes to the disjoining pressure in Equation (3.2), namely, $\Pi = \Pi_{vdW}$. When the contact angle is more than 40°, the hydrophobic effect should be added into the overall disjoining pressure: $\Pi = \Pi_{vdW} + \Pi_{HB}$.

4.3 Results and Discussion

4.3.1 Contact Angle of Pentlandite after conditioning

Contact angles of captive air bubbles on pentlandite were measured in borax buffer solution with and without conditioning as shown in Figure 4.1. It is noted that for freshly polished

pentlandite and H_2O_2 treated pentlandite, bubble attachment was not observed and it would roll off the surface immediately. The contact angle is considered to be less than 10° and the surface is hydrophilic. Both H_2O_2 and PIBX, and PIBX treatment increased the contact angle and the pentlandite surface changed to a more hydrophobic nature.

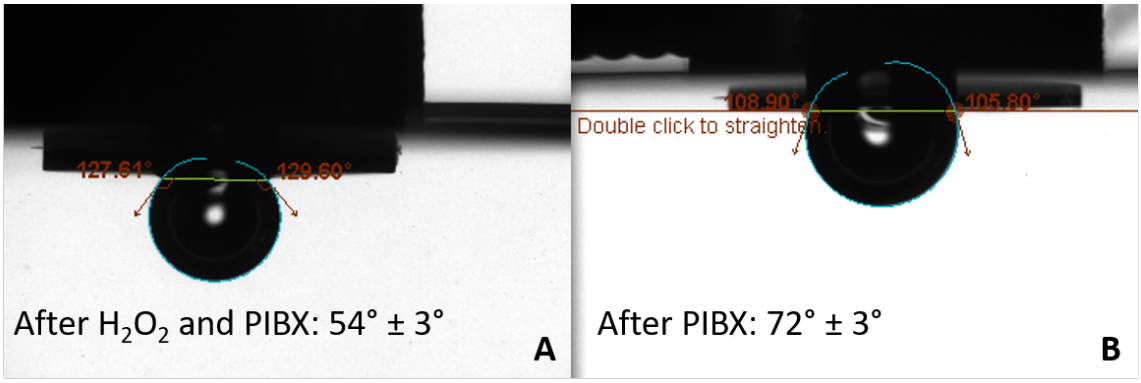

Figure 4.1: Contact angle of a captive bubble on pentlandite (A) after H_2O_2 and PIBX conditioning and (B) after PIBX conditioning.

4.3.2 Topography Images of Pentlandite with or without conditioning

A photograph of typical AFM bubble probe on pentlandite surface accquired from top view camera in AFM head is shown in Figure 4.2 left panel. The smoothness of pentlandite surface was confirmed by the height image on the right panel. It showed no virtual structure except minor scratches from the polishing process. The roughness was found to be around 1.6 nm over a $3 \times 3\ \mu m^2$ area, which is suitable for bubble interaction.[21]

Figure 4.3 shows the representative topography images of treated pentlandite: (A) after H_2O_2 and PIBX conditioning and (B) after PIBX conditioning. Two conditionings resulted in two distinct topography features: (A) granular structure with typical height of 20 nm formed and no polishing scratches could be observed if sample was exposed to H_2O_2 before PIBX; (B) no virtual structure formed but some domains with typical height of 10 nm covered pentlandite, and scratches were still clear after PIBX treatment. Analyzed by

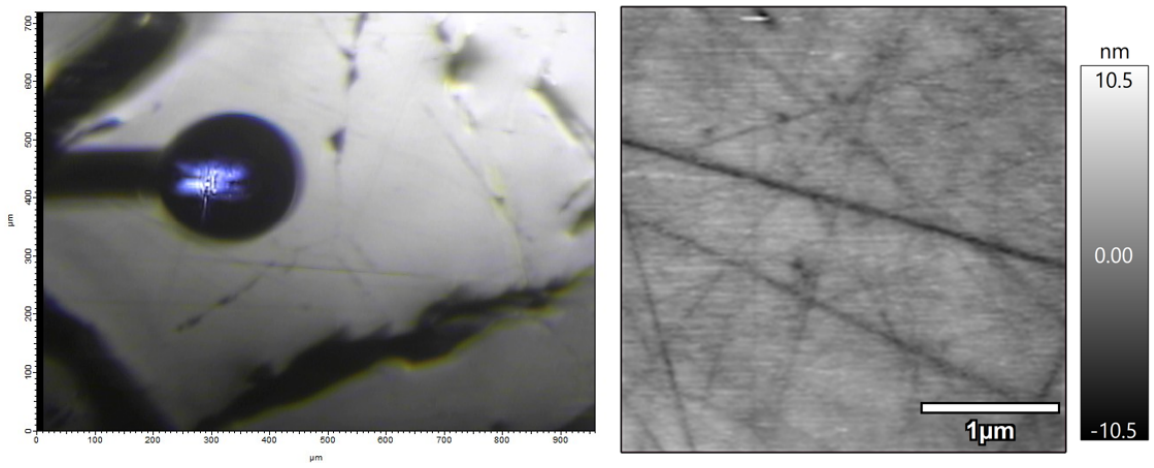

Figure 4.2: (left panel) A typical AFM bubble probe on pentlandite surface from top view camera in AFM head, (right panel) height image of freshly polished pentlandite surface in borax buffer solution.

AFM software, the root mean square roughness (R_q) remained low and similar for both cases, 4.1 nm vs. 3.4 nm. This suggested that the surface became rougher in the presence of H_2O_2.

One potential explanation for the observed asperities in Figure 4.3 A is the formation of metal hydroxide precipitate, though further investigation is warranted. This precipitate nucleated and grew along the scratches from polishing which made the main point to the distinction between Figure 4.3 A & B. The H_2O_2 addition also increased the pulp potential and improved the following formation of metal xanthate complex and dixanthogen from the xanthate conditioning. Metal xanthate complex and dixanthogen are well accepted as hydrophobic species.[87, 88] Accordingly, pentlandite after H_2O_2 and PIBX conditioning is partially hydrophobic (contact angle $\sim 55°$).

As for PIBX treatment, it is speculated that the observed domain could be xanthate chemical adsorbed on pentlandite surface. From the cross-section profile, the height about $5 \sim 8$ nm is consistent with previous findings from Mikhlin et al. [72]. Many previous studies demonstrated that metal xanthate (NiBX) and dixanthogen (BX_2) were formed at

Ni^{2+} sites on pentlandite through chemisorption:[88–90]

$$Pn||Ni^{2+} + 2BX^{-} \rightarrow Pn||Ni - XB + \frac{1}{2}(BX)_2 \tag{4.2}$$

$$Pn|| + X^{-} \rightleftharpoons Pn||X + e^{-} \tag{4.3}$$

$$Pn||X + X^{-} \rightleftharpoons Pn||X_2 + e^{-} \tag{4.4}$$

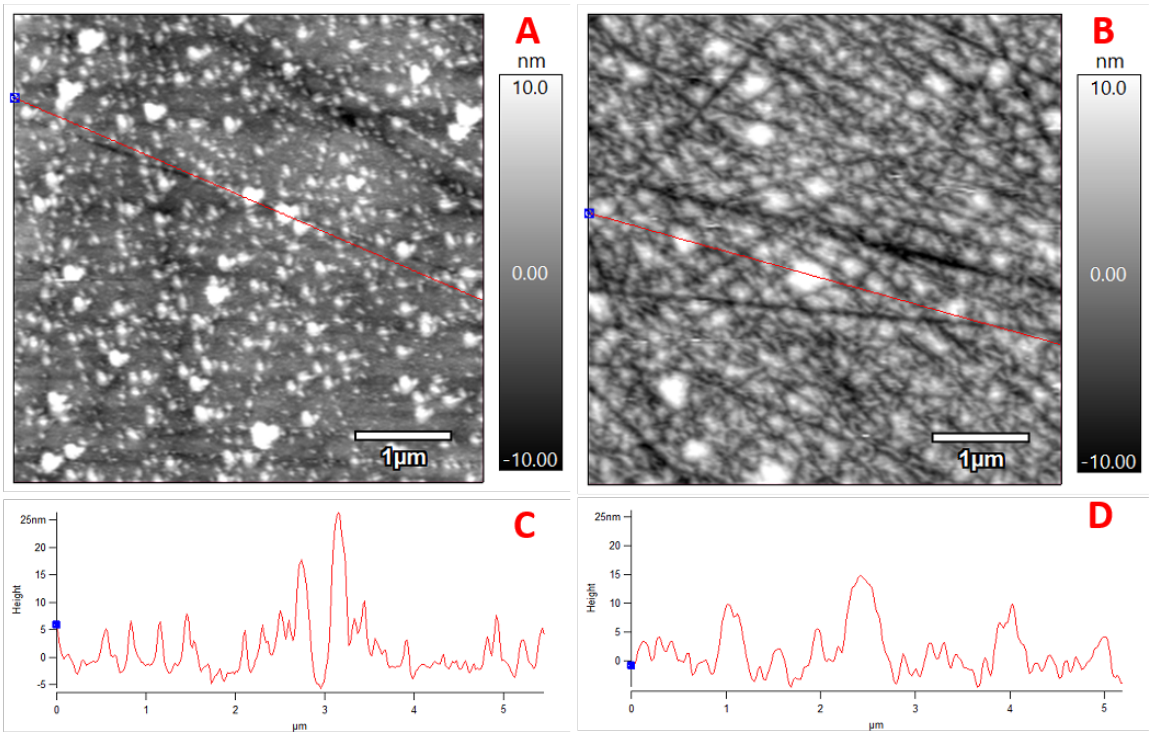

Figure 4.3: Height images of pentlandite in borax buffer solution and corresponding cross-section profile acquired (A) and (C) after H_2O_2 and PIBX conditioning, (B) and (D) after PIBX conditioning.

4.3.3 Interaction Force between Pentlandite and Air Bubble in Borax Buffer Solution

For unreacted pentlandite surface, the bubble probe experienced repulsive force until 20 nN (Figure 4.4 A) and a weak attraction during retraction due to a hydrodynamic suction effect.[57] The Hamaker constant for air-water-pentlandite system is calculated to be - 2.09×10^{-21} J according to the Hamaker constant for pentlandite in vacuum as 3.3×10^{-20} J.[91] The negative value of the Hamaker constant indicates repulsive vdW force. Since pentlandite shows hydrophilic property without any conditioning, only repulsive vdW force operates for the equilibrium interaction force. SRYL model (red solid line) incorporating the vdW effect exhibited good agreement with the experimental result (blue open symbols) as presented in Figure 4.4 A. Figure 4.4 B displays the corresponding disjoining pressure. The water film between air bubble and freshly polished pentlandite stopped thinning around 5 nm. Because no attractive force acted in this case, the repulsive vdW force inhibited further bubble attachment from occurring and stabilized the thin film.

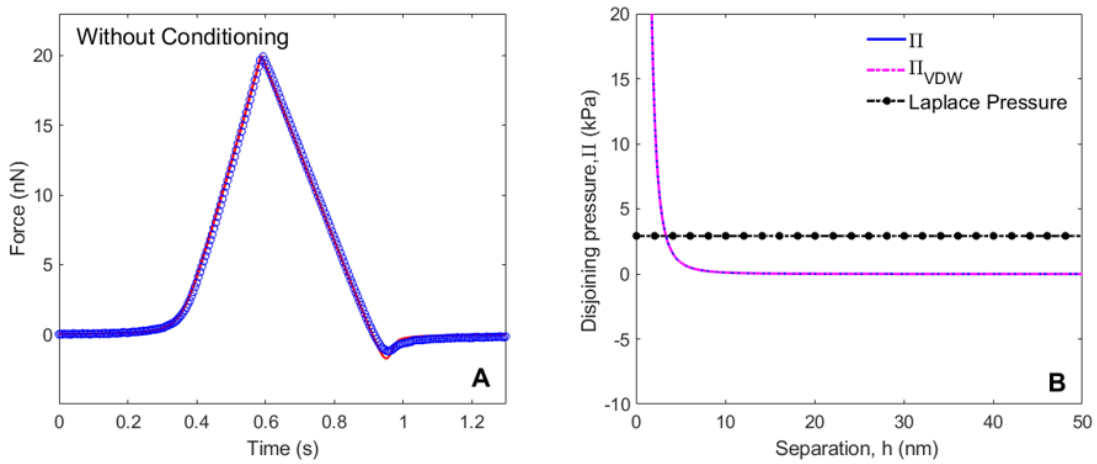

Figure 4.4: (A) Experimental force curve and theoretical calculation for the interaction between bubble and freshly polished pentlandite in borax buffer solution with a driving velocity of 1 μm/s. Open symbols are experimental AFM data and solid line is the theoretical calculation using the SRYL model. (B) Calculated disjoining pressure for this system.

Flotation additive such as xanthate is essential for sulfide mineral flotation. After xanthate conditioning, the interaction force curve between the bubble and pentlandite is presented in Figure 4.5 A. The interaction force experienced a slight repulsion around 3 nN and decreased dramatically until the minimum range of AFM measurement (-300 nN). This suggested several sub-processes: (1) the bubble attached onto pentlandite, (2) the bubble pulled down the cantilever, (3) the thin water film between bubble and surface ruptured, (4) the three phase contact line formed and spread on the surface. All these sub-processes happened spontaneously because of the strong hydrophobicity of PIBX treated pentlandite. After force measurement, the bubble detached from the cantilever. The SRYL model also showed good correlation with experimental data for approaching region as shown in Figure 4.5 B. Taking a contact angle of 72°, the constant $\sigma(1-\cos\theta)$ for hydrophobic interaction can be obtained to be 0.031 N/m. The decay length of hydrophobic interaction was inferred to be 1.2 ± 0.1 nm. From disjoining pressure calculation as displayed in Figure 4.5 C, hydrophobic interaction acted beyond vdW interaction. The critical film thickness was found to be $\leq 12nm$.

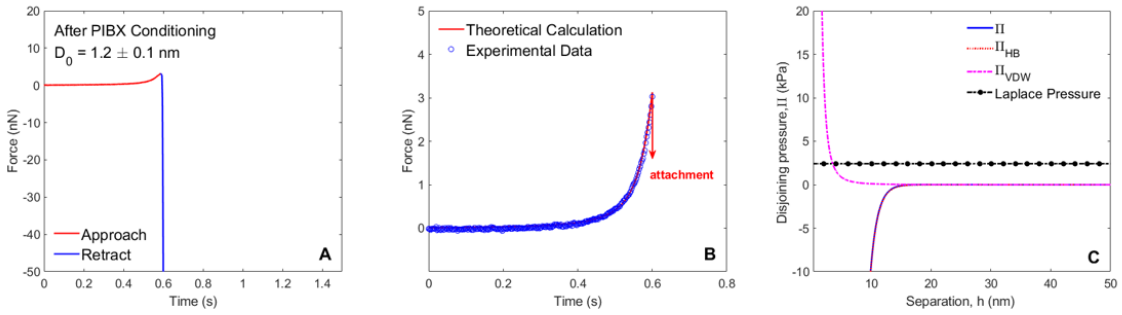

Figure 4.5: (A) Interaction force curve between bubble and PIBX-treated pentlandite in borax buffer solution with a driving velocity of 1 μm/s. (B) Comparison of approaching curve and theoretical calculation. Open symbols are experimental AFM data and solid line is the theoretical calculation using the SRYL model. (C) Calculated disjoining pressure for this system.

H_2O_2 conditioning brought abundant oxidation products and made the pentlandite

rougher as discussed in section 5.3.2. Surface roughness has always been a serious problem for surface force measurement. But the effect of surface roughness in this system is reduced because of the small interaction area by AFM bubble probe (less than $1 \times 1\ \mu m^2$). The interacion force between air bubble and H_2O_2-treated pentlandite is shown in Figure 4.6 A and similar to Figure 4.4. From contact angle measurement, pentlandite shows hydrophilic property and thus vdW force is the only effect considered for the surface force.

The further exposure of H_2O_2-treated pentlandite to PIBX solution resulted in shows a comparable repulsive force (4 nN) during approach (Figure 4.7 A) before point (a) with Figure 4.5 (3.2 nN). This repulsion was due to the repulsive vdW forces. When the attractive hydrophobic force exceeded the spring constant of the cantilever, the bubble jumped into the surface, thin water film ruptured, and the three phase contact line formed. In contrast to the case of PIBX conditioning, force decrease stopped at -30 nN instead of reaching the minimum range of measurement and more repulsive force was observed after jump-in until the applied force reached approximately 7 nN (point (b)). It is possible that the protrusions formed from oxidation conditioning hindered the expansion of TPCL and the capillary bridge formed between cantilever and surface. Upon the retraction of the cantilever (after point (b)), the bubble did not detach from the cantilever and the capillary bridge remained until the cantilever was retracted back to its original position. The total force in the vertical direction between (a) and (b) is balanced by the Laplace pressure force, capillary force, and attachment force:[92]

$$F_t \approx 2\pi r_{tpc}\gamma_{lv}\sin\theta_{att} - \pi r_{tpc}^2\left(\frac{2\gamma_{lv}}{R_c}\right) \tag{4.5}$$

where r_{tpc} is the radius of contact region, γ_{lv} is the interfacial tension of the air/water interface, θ_{att} is the attachment contact angle, R_c is the radius of bubble.

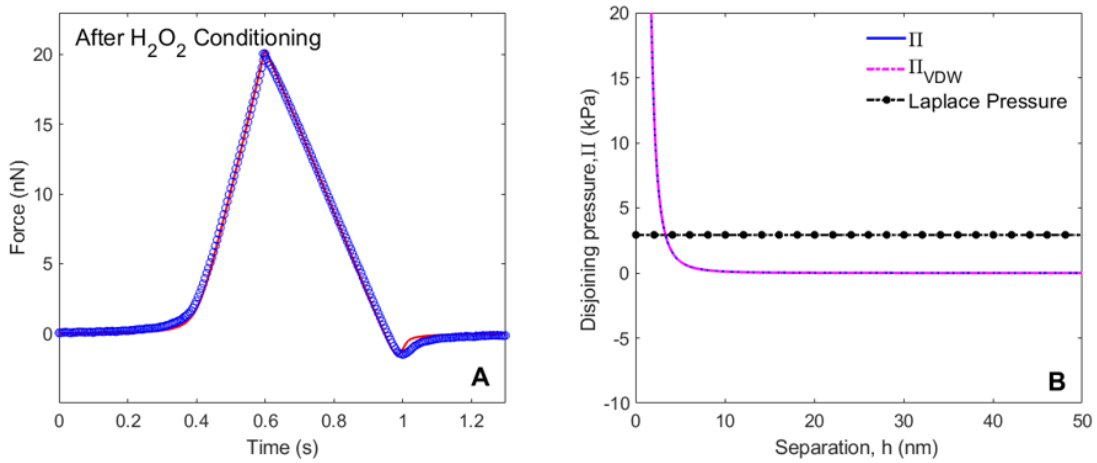

Figure 4.6: (A) Experimental force curve and theoretical calculation for the interaction between bubble and H_2O_2 treated pentlandite in borax buffer solution with a driving velocity of 1 μm/s. Open symbols are experimental AFM data and solid line is the theoretical calculation using the SRYL model. (B) Calculated disjoining pressure for this system.

Nontransparent mineral sample limits the observation of the contact area and the attachment contact angle leading to two unknowns (r_{tpc} and θ_{att}) in Equation (4.5). Moreover, further quantification of the surface forces beyond point (a) requires the exact information about the surface nanoscale structure. There is no reliable model to describe the interaction between air bubble and surface which is both physically and chemically heterogeneous.[1] The SRYL model was built to understand the equilibrium surface force between bubble and surface. It can only successfully predict the bubble behavior before jump-in (point (a)). From the good correlation in Figure 4.7 B, the decay length of hydrophobic force was estimated to be 0.9 ± 0.1 nm. The minimum film thickness prior to attachment was around 9 nm. It is well accepted that surface roughness limits the close approach for two surfaces and thus weakens the interaction force.[93, 94] However, bubble underwent attachment onto pentlandite either after H_2O_2-PIBX conditioning or PIBX conditioning. Hydrophobic force was strong and sufficient to induce the bubble-surface attachment. The effect of protruding nanoscale structure from H_2O_2 oxidation was seemingly overshadowed in

terms of the micron-sized bubble attachment outcome.

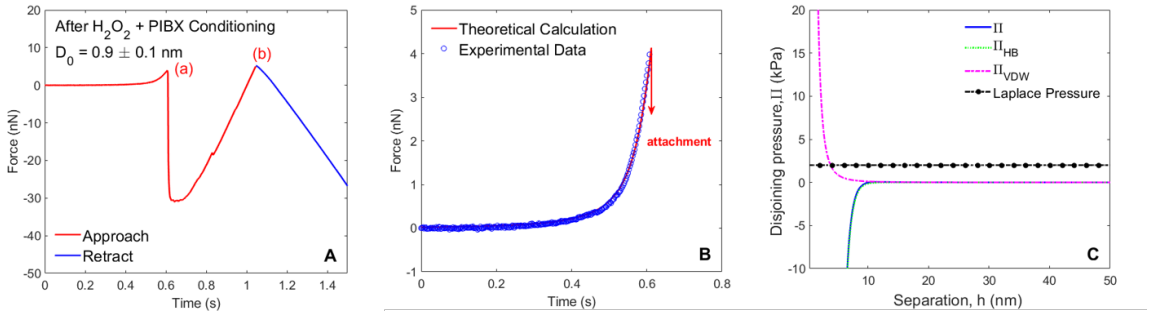

Figure 4.7: (A) Measured forces between bubble and pentlandite after H_2O_2 and PIBX conditioning in borax buffer solution with a driving velocity of 1 μm/s. (A) Open symbols are experimental AFM data and solid line is the theoretical calculation using the SRYL model. (B) Calculated disjoining pressure for this system.

4.3.4 Adhesion Force Map of Pentlandite

In order to understand the chemical characteristics of pentlandite from different conditioning, adhesion force map was performed. Different from force measurement by bubble probe technique and conventional topography imaging, adhesion force map complements the data by providing the force-distance curves between an OTS-tip and pentlandite surface over an area of 2×2 μm^2. It is well accepted that OTS treated silicon nitride tip is hydrophobic where contact angle is around 109°. As discussed in section 5.3.3, only repulsive vdW force and attractive HB force were detectable in this system. Since either observed asperity or xanthate adsorption layer are thin, the contribution from vdW effect stays roughly constant. The variation measured from adhesion force map is ascribed to the hydrophobicity of the pentlandite surface. Numerous attempt has been on the adhesion force between hydrophobic surfaces over the past several decades.[95–99] Bright color from the adhesion force map represent low-adhesion domain corresponding to hydrophilic region. Grey color represent high adhesion between OTS-tip and surface indicating hydrophobic regions. By collecting and analyzing the force data from adhesion

force map, the histogram was produced and presented in the right panel. It illustrates the adhesion forces distribution which are normalized by assuming the radius of OTS-tip spherical cap, 20 nm.

Figure 4.8 and Figure 4.9 show the adhesion force map obtained from untreated and H_2O_2-treated pentlandite sample in borax buffer solution. At 20 nN scale, both of images show generally gray color indicating hydrophilic nature of the surfaces. These are consistent with contact angle and force measurement. Majority of adhesion force are found to be less than 50 mN/m (right panel), in agreement with the hydrophilic domain from Xie's work.[99]

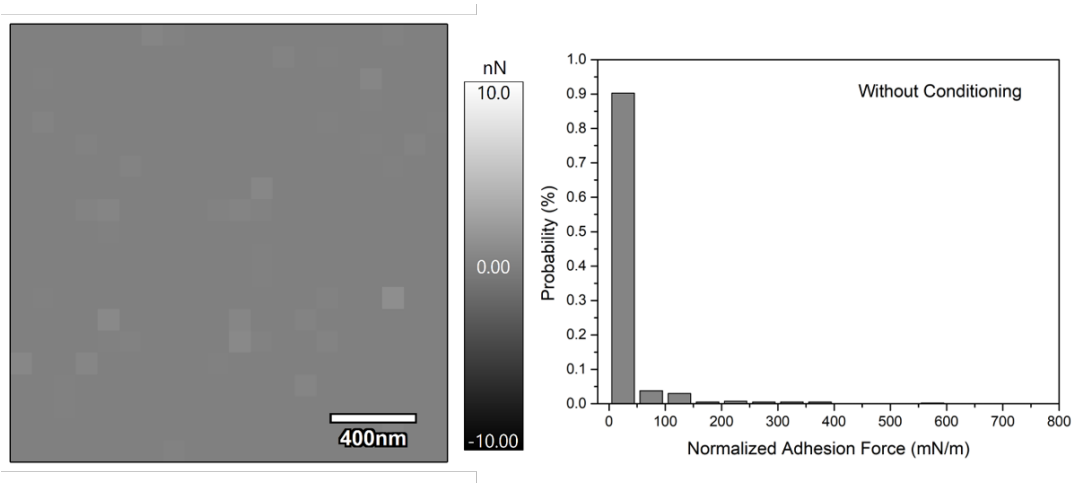

Figure 4.8: (left panel) Adhesion force map obtained from freshly polished pentlandite. (right panel) Histogram of corresponding adhesion force distribution.

After xanthate treatment, the pentlandite sample exhibits remarkable adhesion to the hydrophobic tip regardless of the H_2O_2 addition, as many bright points observed in Figure 4.10 and Figure 4.11. However, the adhesion force map for the H_2O_2 and PIBX treated pentlandite is more hetergeneous than Figure 4.11 and reveals some micron-sized hydrophobic domains where bright points are connected. The corresponding distribution of adhesion is skewed below 100 mN/m with the rest falls in the range of 100 $\sim$ 300 mN/m. It is suggested here that these hydrophobic micron domains may contribute to the

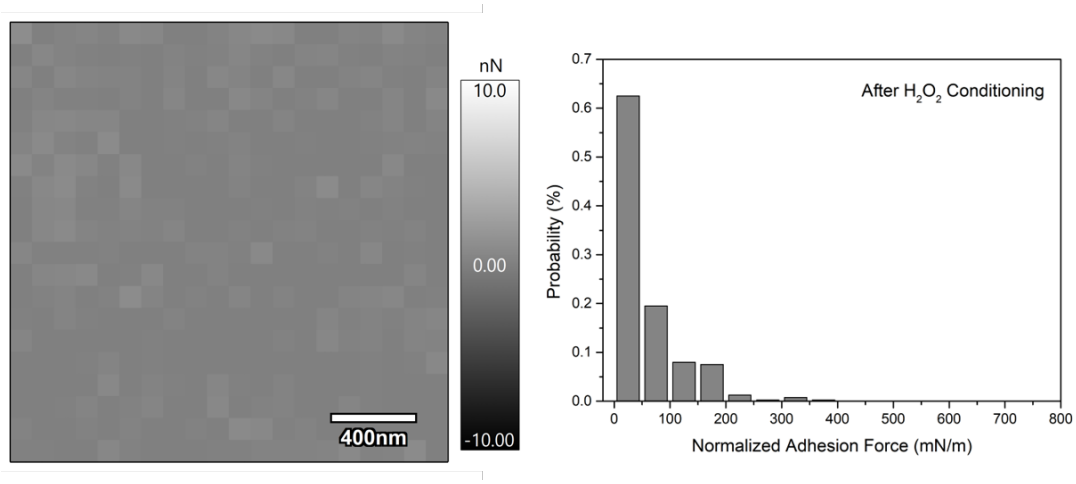

Figure 4.9: (left panel) Adhesion force map obtained from H_2O_2 treated pentlandite. (right panel) Histogram of corresponding adhesion force distribution.

increased hydrophobicity of pentlandite and induce the bubble attachment.

For the data set measured from the pentlandite sample which was directly exposed to PIBX, (Figure 4.11), the overall image show brighter color and the maximum probability of adhesion force centered between 200 $\sim$ 300 mN/m which is higher than other cases. Additionally, the adhesion force map is less chemically heterogeneous, which coincides with the readily bubble attachment from section 5.3.3.

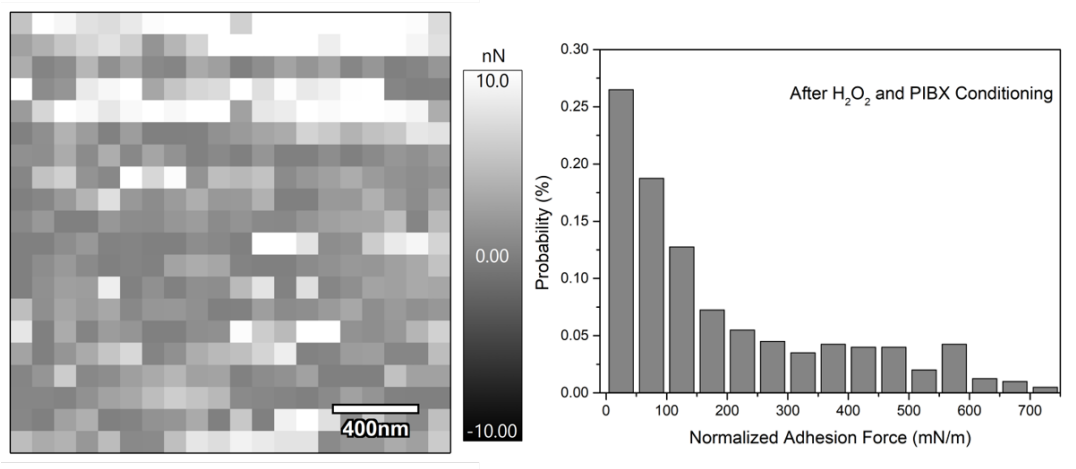

Figure 4.10: (left panel) Adhesion force map obtained from H_2O_2 and PIBX treated pentlandite. (right panel) Histogram of corresponding adhesion force distribution.

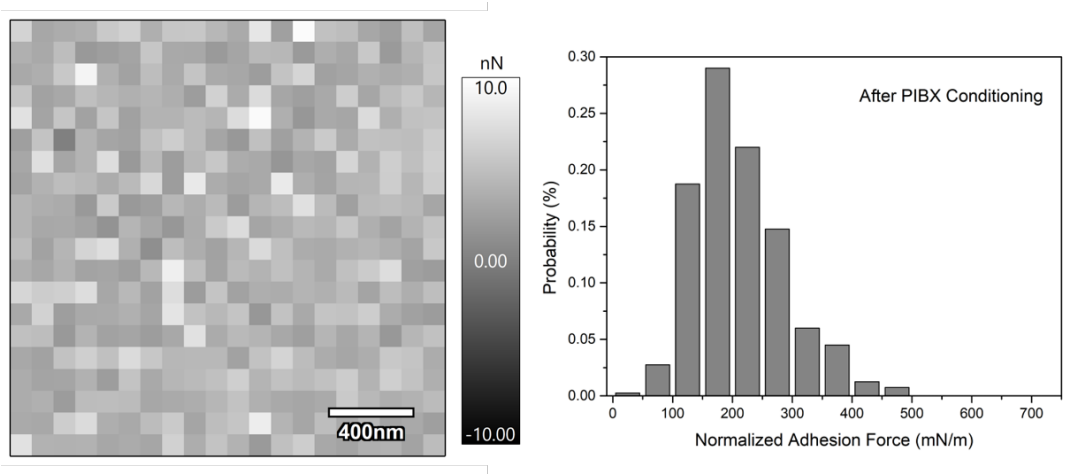

Figure 4.11: (left panel) Adhesion force map obtained from PIBX treated pentlandite. (right panel) Histogram of corresponding adhesion force distribution.

4.4 Conclusion

The AFM bubble probe technique, topography images, adhesion force map together with contact angle measurement were utilized to estimate the impact of oxidation using H_2O_2 solution on the wettability and surface properties of pentlandite in borax buffer solution. The additive of H_2O_2 did not alter the hydrophilicity but increased the surface roughness by introducing nanoscale asperities onto pentlandite. Combined with PIBX treatment, pentlandite shows chemical heterogeneity and partial hydrophobicity but still allows for bubble attachment. When pentlandite underwent direct xanthate treatment, it showed less chemical heterogeneity and stronger hydrophobicity, and micron-sized bubble attachment can be readily induced as desired.

The present study produced a satisfying correlation between the SRYL model and the interaction forces between air bubble and pentlandite. For untreated and H_2O_2-treated pentlandite, vdW forces was responsible for the repulsion. The introduction of PIBX allowed the attractive HB forces to dominate and repulsive vdW forces were negligible. The characteristic lengths of HB forces were found to be 0.9 ± 0.1 nm and 1.2 ± 0.1 nm for

H_2O_2-PIBX treated pentlandite, and PIBX treated pentlandite, respectively. In addition, the chemical properties of pentlandite was well-characterized at nanoscale by adhesion force map.

As a whole, these results suggest that the additive of H_2O_2 presents a promising method for selectivity of pentlandite and pyrrhotite, and warrants further investigation.

Chapter 5

Conclusion and Recommendations for Future Work

5.1 Conclusions

In this thesis, AFM deformable drop/bubble probe technique was successfully applied to understand surface forces and interaction mechanisms for three colloidal systems in mineral flotation: (a) oil droplet and molybdenite, (b) bubble and millerite, and (c) bubble and pentlandite.

The key findings of this work can be summarized as:

1. The interaction force between dodecane oil droplet and molybdenite was directly measured by the AFM droplet probe technique. The Stokes-Reynolds-Young-Laplace model was compared with experimental data obtained under various aqueous conditions and provided insight into the impact of VDW, EDL, and HB forces for each experimental condition. At high pH and low salinity, both the oil droplet and the molybdenite surface were strongly negatively charged, arising from the

adsorption of hydroxyl ions originating from the water. Under these conditions, strong EDL repulsion dominated and no oil attachment was observed. By contrast, low pH and high salinity are conducive to the attachment of oil to molybdenite due to a suppression of surface potential and Debye length, respectively, which both reduced repulsive EDL forces.

2. The SRYL model provide a complete description of the thin water film drainage process under different aqueous solutions. The hydrophobic attraction was quantified with an exponential decay length of 1.0 ± 0.1 nm.

3. The stability map was plotted in term of salt concentration, pH value, NaCl, and $CaCl_2$ solutions. Ca^{2+} exerted a stronger effect on the attachment behavior between the oil droplet and molybdenite basal plane than Na^+ at the same ionic strength.

4. The wettability and surface potential of millerite under pH 4 and pH 12 were investigated using the AFM bubble probe technique. Experimental data suggested that acidic condition favors bubble-millerite attachment while reaction production from pH 12 impart millerite surface less hydrophobic than in pH 4. Apart from AFM force measurement, the SRYL model was employed and exhibited good agreement with experimental results. This has led to an extensive understanding in terms of surface forces.

5. The AFM bubble probe technique, topography images, adhesion force map together with contact angle measurement are utilized to estimate the impact of oxidation using H_2O_2 solution on the wettability and surface properties of pentlandite in borax buffer solution. The additive of H_2O_2 did not alter the hydrophilicity but increased the surface roughness by introducing nanoscale asperities onto pentlandite.

Combined with PIBX treatment, pentlandite shows chemical heterogeneity and partial hydrophobicity but still allows for the bubble attachment.

6. When pentlandite underwent direct xanthate treatment, it showed less chemical heterogeneity and stronger hydrophobicity than H_2O_2-PIBX treated pentlandite. Micron-sized bubble attachment can be readily induced as desired.

7. The validated SRYL model revealed the interaction forces between air bubble and pentlandite. For untreated and H_2O_2-treated pentlandite, vdW forces was responsible for the repulsion. The introduction of PIBX allowed the attractive HB forces to dominate and repulsive vdW forces were negligible. The characteristic lengths of HB force were found to be 0.9 ± 0.1 nm and 1.2 ± 0.1 nm for H_2O_2-PIBX treated pentlandite and PIBX treated pentlandite, respectively. Since bubble attachment can be induced where H_2O_2 are present and absent, H_2O_2 appears to be a promising candidate for selectivity of pentlandite and pyrrhotite.

5.2 Recommendations for future work

1. The present study mainly studied the effect of oxidation on bubble attachment onto pentlandite. In order to determine the species that contributed to the increase in surface roughness, further investigation is warranted. One possible way to accomplish this is to characterize the element composition by X-ray Photoelectron Spectroscopy (XPS) or other characterization techniques, including Fourier-transform Infrared Spectroscopy (FTIR) and Time-of-Flight Secondary Ion Mass Spectrometry (ToF-SIMS).

2. It is recommended that more experiments be completed on pyrrhotite following the

same procedures conducted in this study. Further force measurement by bubble probe pyrrhotite are worthwhile to repeat if fresh smooth pyrrhotite sample is guaranteed. Comparing present study with further results regarding pyrrhotite will provide promising method in improving the selectivity of pentlandite and pyrrhotite, and valuable insight into the underlying mechanisms.

3. It is recommended that experiments be undertaken with other additives in mineral flotation: collectors, surfactants, dissolved gas, metal ions for activation, etc.

4. This bubble probe technique is also applicable for characterizing the surfaces or interfaces charging behaviors. Rico et al. have revealed the pH-dependent surface potential of the air/water interface and anomalous stability of carbon dioxide bubble in aqueous solutions.[26] Utilizing similar idea, the presence of gold oxide can change the surface potential dramatically and increase the isoelectric points by 2 pH units.[100] As mentioned in this study, the surface potential of oil/water interface, air/water interface and molybdenite surface in various aqueous solutions were well estimated by the AFM bubble probe technique assisted with the validated SRYL model. This methodology can offer a rigorous prediction of the surface potential in diverse colloidal systems.

References

[1] Ralston, D. Fornasiero, and R. Hayes. Bubble-particle attachment and detachment in flotation. *International Journal of Mineral Processing*, pages 1–32, (1999).

[2] B. Wang and Y. Peng. The effect of saline water on mineral flotation - A critical review. *Minerals Engineering*, 66:13–24, (2014). doi:10.1016/j.mineng.2014.04.017.

[3] Y. Xing, X. Gui, L. Pan, B. E. Pinchasik, Y. Cao, J. Liu, M. Kappl, and H. J. Butt. Recent experimental advances for understanding bubble-particle attachment in flotation. *Advances in Colloid and Interface Science*, 246(May):105–132, (2017). doi:10.1016/j.cis.2017.05.019.

[4] Z. Dai, D. Fornasiero, and J. Ralston. Particle-bubble collision models - a review. *Advances in Colloid and Interface Science*, 85(2):231–256, (2000). doi:10.1016/S0001-8686(99)00030-5.

[5] G. Wang, A. V. Nguyen, S. Mitra, J. B. Joshi, G. J. Jameson, and G. M. Evans. A review of the mechanisms and models of bubble-particle detachment in froth flotation. *Separation and Purification Technology*, 170:155–172, (2016). doi:10.1016/j.seppur.2016.06.041.

[6] A. V. Nguyen, D. A. An-Vo, T. Tran-Cong, and G. M. Evans. A review of stochastic description of the turbulence effect on bubble-particle interactions in flotation. *International Journal of Mineral Processing*, 156:75–86, (2016). doi:10.1016/j.minpro.2016.05.002.

[7] J. Wang, L. Xie, Q. Liu, and H. Zeng. Effects of salinity on xanthate adsorption on sphalerite and bubble-sphalerite interactions. *Minerals Engineering*, 77:34–41, (2015). doi:10.1016/j.mineng.2015.02.009.

[8] R. Woods. The oxidation of ethyl xanthate on platinum, gold, copper, and galena electrodes. Relation to the mechanism of mineral flotation. *Journal of Physical Chemistry*, 75(3):354–362, (1971). doi:10.1021/j100673a011.

[9] P. Bonnissel-Gissinger, M. Alnot, J. J. Ehrhardt, and P. Behra. Surface oxidation of pyrite as a function of pH. *Environmental Science and Technology*, 32(19):2839–2845, (1998). doi:10.1021/es980213c.

[10] G. Wittstock, I. Kartio, D. Hirsch, S. Kunze, and R. Szargan. Oxidation of Galena in Acetate Buffer Investigated by Atomic Force Microscopy and Photoelectron Spectroscopy. *Langmuir*, 12(23):5709–5721, (2002). doi:10.1021/la960385s.

[11] P. Clarke, D. Fornasiero, J. Ralston, and R. S. C. Smart. A study of the removal of oxidation products from sulfide mineral surfaces. *Minerals Engineering*, 8(11): 1347–1357, (1995).

[12] S. Chander. Electrochemistry of sulfide mineral flotation. *Mining, Metallurgy & Exploration & Exploration*, 5(3):104–114, (1988). doi:10.1007/bf03402498.

[13] P. J. Guy and W. J. Trahar. The influence of grinding and flotation environments on the laboratory batch flotation of galena. *International Journal of Mineral Processing*, 12 (1-3):15–38, (1984).

[14] S. Chander and D. W. Fuerstenau. On the natural floatability of molybdenite. *Trans. AIME*, 252:62–69, (1972).

[15] A. V. Nguyen, H. J. Schulze, and J. Ralston. Elementary steps in particle—bubble attachment. *International Journal of Mineral Processing*, 51(1-4):183–195, (1997).

[16] I. Sven-Nilsson. Effect of contact time between mineral and air bubbles on flotation. *Kol loid*, 230, (1934).

[17] G. Gu, Z. Xu, K. Nandakumar, and J. Masliyah. Effects of physical environment on induction time of air–bitumen attachment. *International Journal of Mineral Processing*, 69(1-4):235–250, (2003).

[18] M. Ejtemaei and A. V. Nguyen. A comparative study of the attachment of air bubbles onto sphalerite and pyrite surfaces activated by copper sulphate. *Minerals Engineering*, 109:14–20, (2017). doi:10.1016/j.mineng.2017.02.008.

[19] W. A. Ducker, Z. Xu, and J. N. Israelachvili. Measurements of Hydrophobic and DLVO Forces in Bubble–Surface Interactions in Aqueous Solutions. *Langmuir*, 10(9): 3279–3289, (1994). doi:10.1021/la00021a061.

[20] R. R. Dagastine, R. Manica, S. L. Carnie, D. Y. C. Chan, G. W. Stevens, and F. Grieser. Dynamic forces between two deformable oil droplets in water. *Science*, 313(5784): 210–213, (2006). doi:10.1126/science.1125527.

[21] D. Y. Chan, E. Klaseboer, and R. Manica. Film drainage and coalescence between deformable drops and bubbles. *Soft Matter*, 7(6):2235–2264, (2011). doi:10.1039/c0sm00812e.

[22] R. F. Tabor, R. Manica, D. Y. Chan, F. Grieser, and R. R. Dagastine. Repulsive Van der Waals forces in soft matter: Why bubbles do not stick to walls. *Physical Review Letters*, 106(6):1–4, (2011). doi:10.1103/PhysRevLett.106.064501.

[23] L. Xie, C. Shi, J. Wang, J. Huang, Q. Lu, Q. Liu, and H. Zeng. Probing the interaction between air bubble and sphalerite mineral surface using atomic force microscope. *Langmuir*, 31(8):2438–2446, (2015). doi:10.1021/la5048084.

[24] L. Xie, J. Wang, D. Yuan, C. Shi, X. Cui, H. Zhang, Q. Liu, Q. Liu, and H. Zeng. Interaction Mechanisms between Air Bubble and Molybdenite Surface: Impact of Solution Salinity and Polymer Adsorption. *Langmuir*, 33(9):2353–2361, (2017). doi:10.1021/acs.langmuir.6b04611.

[25] R. F. Tabor, C. Wu, H. Lockie, R. Manica, D. Y. Chan, F. Grieser, and R. R. Dagastine. Homo- and hetero-interactions between air bubbles and oil droplets measured by atomic force microscopy. *Soft Matter*, 7(19):8977–8983, (2011). doi:10.1039/c1sm06006f.

[26] R. F. Tabor, D. Y. C. Chan, F. Grieser, and R. R. Dagastine. Anomalous stability of carbon dioxide in pH-controlled bubble coalescence. *Angewandte Chemie - International Edition*, 50(15):3454–3456, (2011). doi:10.1002/anie.201006552.

[27] H. Lockie, R. Manica, R. F. Tabor, G. W. Stevens, F. Grieser, D. Y. C. Chan, and R. R. Dagastine. Anomalous pull-off forces between surfactant-free emulsion drops in different aqueous electrolytes. *Langmuir*, 28(9):4259–4266, (2012). doi:10.1021/la204753y.

[28] R. F. Tabor, C. Wu, F. Grieser, R. R. Dagastine, and D. Y. C. Chan. Measurement of the hydrophobic force in a soft matter system. *Journal of Physical Chemistry Letters*, 4 (22):3872–3877, (2013). doi:10.1021/jz402068k.

[29] C. Shi, B. Yan, L. Xie, L. Zhang, J. Wang, A. Takahara, H. Zeng, B. Yan, L. Zhang, A. Takahara, C. Shi, L. Xie, B. Yan, L. Xie, L. Zhang, J. Wang, A. Takahara, H. Zeng, B. Yan, L. Zhang, A. Takahara, C. Shi, and L. Xie. Long-Range Hydrophilic Attraction between Water and Polyelectrolyte Surfaces in Oil. *Angewandte Chemie - International Edition*, 55(48):15017–15021, (2016). doi:10.1002/anie.201608219.

[30] C. Shi, L. Zhang, L. Xie, X. Lu, Q. Liu, J. He, C. A. Mantilla, F. G. Van Den Berg, and H. Zeng. Surface Interaction of Water-in-Oil Emulsion Droplets with Interfacially Active Asphaltenes. *Langmuir*, 33(5):1265–1274, (2017). doi:10.1021/acs.langmuir.6b04265.

[31] E. J. Jamieson, C. J. Fewkes, J. D. Berry, and R. R. Dagastine. Forces between oil drops in polymer-surfactant systems: Linking direct force measurements to microfluidic observations. *Journal of Colloid and Interface Science*, 544:130–143, (2019). doi:10.1016/j.jcis.2019.02.051.

[32] C. Shi, X. Cui, X. Zhang, P. Tchoukov, Q. Liu, N. Encinas, M. Paven, F. Geyer, D. Vollmer, Z. Xu, H. J. Butt, and H. Zeng. Interaction between Air Bubbles and

Superhydrophobic Surfaces in Aqueous Solutions. *Langmuir*, 31(26):7317–7327, (2015). doi:10.1021/acs.langmuir.5b01157.

[33] M. C. Fuerstenau, G. J. Jameson, and R.-H. Yoon. *Froth flotation: a century of innovation*. SME, (2007). ISBN 0873352521.

[34] S. Song, X. Zhang, B. Yang, and A. Lopez-Mendoza. Flotation of molybdenite fines as hydrophobic agglomerates. *Separation and Purification Technology*, 98:451–455, (2012). doi:10.1016/j.seppur.2012.06.016.

[35] S. Song and A. Lopez-Valdivieso. Computational studies on interaction between air bubbles and hydrophobic mineral particles covered by nonpolar oil. *Journal of Colloid and Interface Science*, 212(1):42–48, (1999). doi:10.1006/jcis.1998.6012.

[36] Q. quan Lin, G. hua Gu, H. Wang, Y. cai Liu, J. gang Fu, C. qing Wang, Q. quan Lin, G. hua Gu, H. Wang, Y. cai Liu, J. gang Fu, and C. qing Wang. Flotation mechanisms of molybdenite fines by neutral oils. *International Journal of Minerals, Metallurgy and Materials*, 25(1):1–10, (2018). doi:10.1007/s12613-018-1540-8.

[37] A. Liu, M. qiang Fan, Z. hong Li, and J. chuan Fan. Non-polar oil assisted DDA flotation of quartz I: Interfacial interaction between dodecane oil drop and mineral particle. *International Journal of Mineral Processing*, 168:1–8, (2017). doi:10.1016/j.minpro.2017.09.004.

[38] L. Wang and R. H. Yoon. Effects of surface forces and film elasticity on foam stability. *International Journal of Mineral Processing*, 85(4):101–110, (2008). doi:10.1016/j.minpro.2007.08.009.

[39] Y. Xing, X. Gui, F. Karakas, and Y. Cao. Role of Collectors and Depressants in Mineral Flotation: A Theoretical Analysis Based on Extended DLVO Theory. *Minerals*, 7(11): 223, (2017). doi:10.3390/min7110223.

[40] X. Cui, C. Shi, S. Zhang, L. Xie, J. Liu, D. Jiang, and H. Zeng. Probing the Effect of Salinity and pH on Surface Interactions between Air Bubbles and Hydrophobic Solids: Implications for Colloidal Assembly at Air/Water Interfaces. *Chemistry - An Asian Journal*, 12(13):1568–1577, (2017). doi:10.1002/asia.201700388.

[41] X. Cui, J. Liu, L. Xie, J. Huang, Q. Liu, J. N. Israelachvili, and H. Zeng. Modulation of Hydrophobic Interaction by Mediating Surface Nanoscale Structure and Chemistry, not Monotonically by Hydrophobicity. *Angewandte Chemie - International Edition*, 57 (37):11903–11908, (2018). doi:10.1002/anie.201805137.

[42] J. L. Parker, P. M. Claesson, and P. Attard. Bubbles, cavities, and the long-ranged attraction between hydrophobic surfaces. *Journal of Physical Chemistry®*, 98(34): 8468–8480, (1994). doi:10.1021/j100085a029.

[43] J. Israelachvili and R. Pashley. The hydrophobic interaction is long range, decaying exponentially with distance. *Nature*, 300(November):341–342, (1982).

[44] Y.-h. Tsao, D. F. Evans, and H. Wennerstrom. Long-Range Attractive Force Between Hydrophobic Surfaces Observed by Atomic Force Microscopy. *Science*, 262(5133): 547–550, (1993).

[45] L. R. Pratt and D. Chandler. Theory of the hydrophobic effect. *The Journal of chemical physics*, 67(8):3683–3704, (1977).

[46] W. A. Ducker and D. Mastropietro. Forces between extended hydrophobic solids: Is there a long-range hydrophobic force? *Current Opinion in Colloid and Interface Science*, 22:51–58, (2016). doi:10.1016/j.cocis.2016.02.006.

[47] C. Shi, X. Cui, L. Xie, Q. Liu, D. Y. Chan, J. N. Israelachvili, and H. Zeng. Measuring forces and spatiotemporal evolution of thin water films between an air bubble and solid surfaces of different hydrophobicity. *ACS Nano*, 9(1):95–104, (2015). doi:10.1021/nn506601j.

[48] H. J. Lockie, R. Manica, G. W. Stevens, F. Grieser, D. Y. Chan, and R. R. Dagastine. Precision AFM measurements of dynamic interactions between deformable drops in aqueous surfactant and surfactant-free solutions. *Langmuir*, 27(6):2676–2685, (2011). doi:10.1021/la1049088.

[49] I. U. Vakarelski, J. Lee, R. R. Dagastine, D. Y. Chan, G. W. Stevens, and F. Grieser. Bubble colloidal AFM probes formed from ultrasonically generated bubbles. *Langmuir*, 24(3):603–605, (2008). doi:10.1021/la7032059.

[50] H. Ding, S. Mettu, R. R. Dagastine, S. H. Rahman, S. Metu, R. R. Dagastine, S. H. Rahman, S. Mettu, R. R. Dagastine, S. H. Rahman, S. Metu, R. R. Dagastine, and S. H. Rahman. Ion Tuned Water Can Greatly Enhance Alteration of Carbonate Surface to Water-wet. In *Unconventional Resources Technology Conference, Houston, Texas, 23-25 July 2018*, pages 1495–1506. Society of Exploration Geophysicists, American Association of Petroleum, (2018). doi:10.15530/urtec-2018-2902143.

[51] L. Xie, J. Wang, J. Huang, X. Cui, X. Wang, Q. Liu, H. Zhang, Q. Liu, and H. Zeng. Anisotropic Polymer Adsorption on Molybdenite Basal and Edge Surfaces and Interaction Mechanism With Air Bubbles. *Frontiers in Chemistry*, 6(August):1–11, (2018). doi:10.3389/fchem.2018.00361.

[52] S. Mettu, J. D. Berry, and R. R. Dagastine. Charge and Film Drainage of Colliding Oil Drops Coated with the Nonionic Surfactant $C_{12}E_5$. *Langmuir*, 33(20):4913–4923, (2017). doi:10.1021/acs.langmuir.6b04632.

[53] S. Mettu, C. Wu, and R. R. Dagastine. Dynamic forces between emulsified water drops coated with Poly-Glycerol-Poly-Ricinoleate (PGPR) in canola oil. *Journal of Colloid and Interface Science*, 517:166–175, (2018). doi:10.1016/j.jcis.2018.01.104.

[54] J. L. Hutter and J. Bechhoefer. Calibration of atomic-force microscope tips. *Review of Scientific Instruments*, 64(7):1868–1873, (1993). doi:10.1063/1.1143970.

[55] O. Manor, I. U. Vakarelski, G. W. Stevens, F. Grieser, R. R. Dagastine, and D. Y. C. Chan. Hydrodynamic Boundary Conditions and Dynamic Forces between Bubbles and Surfaces. *Langmuir*, 24(20):11533–11543, (2008). doi:10.1021/la802206q.

[56] F. Lucay, L. A. Cisternas, E. D. Gálvez, and A. López-Valdivieso. Study of the natural floatability of molybdenite fines in saline solutions and effect of gypsum precipitation. *Mining, Metallurgy & Exploration*, 32(4):203–208, (2018). doi:10.1007/bf03402476.

[57] I. U. Vakarelski, R. Manica, X. Tang, S. J. O'Shea, G. W. Stevens, F. Grieser, R. R. Dagastine, and D. Y. C. Chan. Dynamic interactions between microbubbles in water. *Proceedings of the National Academy of Sciences*, 107(25):11177–11182, (2010). doi:10.1073/pnas.1005937107.

[58] D. G. Goodall, M. L. Gee, and G. W. Stevens. An imaging reflectometry study of the effect of electrolyte on the drainage and profile of an aqueous film between an oil droplet and a hydrophilic silica surface. *Langmuir*, 18(12):4729–4735, (2002). doi:10.1021/la015663o.

[59] Z. Lu, Q. Liu, Z. Xu, and H. Zeng. Probing Anisotropic Surface Properties of Molybdenite by Direct Force Measurements. *Langmuir*, 31(42):11409–11418, (2015). doi:10.1021/acs.langmuir.5b02678.

[60] K. G. Marinova, R. G. Alargova, N. D. Denkov, O. D. Velev, D. N. Petsev, I. B. Ivanov, and R. P. Borwankar. Charging of Oil-Water Interfaces Due to Spontaneous Adsorption of Hydroxyl Ions. *Langmuir*, 12(8):2045–2051, (1996). doi:10.1021/la950928i.

[61] T. Hirajima, G. P. W. Suyantara, O. Ichikawa, A. M. Elmahdy, H. Miki, and K. Sasaki. Effect of Mg^{2+} and Ca^{2+} as divalent seawater cations on the floatability of molybdenite and chalcopyrite. *Minerals Engineering*, 96-97:83–93, (2016). doi:10.1016/j.mineng.2016.06.023.

[62] S. Raghavan and L. L. Hsu. Factors affecting the flotation recovery of molybdenite from porphyry copper ores. *International Journal of Mineral Processing*, 12(1-3):145–162, (1984). doi:10.1016/0301-7516(84)90026-7.

[63] R. F. Tabor, F. Grieser, R. R. Dagastine, and D. Y. Chan. Measurement and analysis of forces in bubble and droplet systems using AFM. *Journal of Colloid and Interface Science*, 371(1):1–14, (2012). doi:10.1016/j.jcis.2011.12.047.

[64] J. D. Berry and R. R. Dagastine. Mapping coalescence of micron-sized drops and bubbles. *Journal of Colloid and Interface Science*, 487:513–522, (2017). doi:10.1016/j.jcis.2016.10.040.

[65] M. R. Hoover. Water Chemistry Effects in the Flotation of Sulfide Ores– a Review and Discussion for Molybdenite. *Complex Sulphide Ores*, pages 100–112, (1980).

[66] Y. Li, C. Lartey, S. Song, Y. Li, and A. R. Gerson. The fundamental roles of monovalent and divalent cations with sulfates on molybdenite flotation in the absence of flotation reagents. *RSC Advances*, 8(41):23364–23371, (2018). doi:10.1039/C8RA02690D.

[67] H. Wan, W. Yang, W. Cao, T. He, Y. Liu, J. Yang, L. Guo, and Y. Peng. The Interaction between Ca^{2+} and Molybdenite Edges and Its Effect on Molybdenum Flotation. *Minerals*, 7(8):141, (2017). doi:10.3390/min7080141.

[68] V. A. Parsegian and D. Gingell. On the electrostatic interaction across a salt solution between two bodies bearing unequal charges. *Biophysical journal*, 12(9):1192–1204, (1972).

[69] M. Xu, F. D. Ford, Z. Dai, V. Lawson, C. Mill, and C. Cliff. Millerite and Its Impact on Cu/Ni Separation. In *43rd Annual Meeting of the Canadian Mineral Processors*, number January 2011, pages 319–330, (2011).

[70] X. Xiong, X. Lu, G. Li, H. Cheng, Q. Xu, and S. Li. Ab Initio Study on the Oxidation Mechanism of Millerite. In *TMS 2019 148th Annual Meeting & Exhibition Supplemental Proceedings*, pages 1037–1044. Springer, (2019).

[71] D. L. Legrand, H. W. Nesbitt, and G. M. Bancroft. X-ray photoelectron spectroscopic study of a pristine millerite (NiS) surface and the effect of air and water oxidation. *American Mineralogist*, 83(12):1256–1265, (1998). doi:10.2138/am-1998-11-1214.

[72] Y. L. Mikhlin, A. A. Karacharov, and M. N. Likhatski. Effect of adsorption of butyl xanthate on galena, PbS, and HOPG surfaces as studied by atomic force microscopy and spectroscopy and XPS. *International Journal of Mineral Processing*, 144:81–89, (2015). doi:10.1016/j.minpro.2015.10.004.

[73] L. Feng, R. Manica, J. S. Grundy, and Q. Liu. Unraveling Interaction Mechanisms between Molybdenite and Dodecane Oil Droplet Using Atomic Force Microscopy. *Langmuir*, 35(18):6024–6031, (2019). doi:10.1021/acs.langmuir.9b00203.

[74] R. R. Dagastine, T. T. Chau, D. Y. Chan, G. W. Stevens, and F. Grieser. Interaction forces between oil-water particle interfaces - Non-DLVO forces. *Faraday Discussions*, 129:111–124, (2005). doi:10.1039/b405750c.

[75] W. Yin, J. Xue, D. Li, Q. Sun, J. Yao, and S. Huang. Flotation of heavily oxidized pyrite in the presence of fine digenite particles. *Minerals Engineering*, 115(November): 142–149, (2018). doi:10.1016/j.mineng.2017.10.016.

[76] C. Yang, T. Dabros, D. Li, J. Czarnecki, and J. H. Masliyah. Measurement of the zeta potential of gas bubbles in aqueous solutions by microelectrophoresis method. *Journal of Colloid and Interface Science*, 243(1):128–135, (2001). doi:10.1006/jcis.2001.7842.

[77] J. Liu, H. Wang, L. Feng, C. Qi, J. Han, B. Xiang, and Q. Liu. Irreversible Surface Evolution of Nickel Sulfide in Aqueous Solution. *In preparation*, 2:1–23, (2019).

[78] H. W. Nesbitt, A. G. Schaufuss, M. Scaini, G. M. Bancroft, and R. Szargan. XPS measurement of fivefold and sixfold coordinated sulfur in pyrrhotites and evidence for millerite and pyrrhotite surface species. *American Mineralogist*, 86(3):318–326, (2001).

[79] C. Wu, K. Nesset, J. Masliyah, and Z. Xu. Generation and characterization of submicron size bubbles. *Advances in Colloid and Interface Science*, 179-182:123–132, (2012). doi:10.1016/j.cis.2012.06.012.

[80] D. L. Legrand, G. M. Bancroft, and H. W. Nesbitt. Oxidation/alteration of pentlandite and pyrrhotite surfaces at pH 9.3: Part 1. Assignment of XPS spectra and chemical trends. *American Mineralogist*, 90(7):1042–1054, (2005). doi:10.2138/am.2005.1691.

[81] V. Malysiak, C. T. O'Connor, J. Ralston, A. R. Gerson, L. P. Coetzer, and D. J. Bradshaw. Pentlandite–feldspar interaction and its effect on separation by flotation. *International journal of mineral processing*, 66(1-4):89–106, (2002).

[82] G. W. Heyes and W. J. Trahar. The flotation of pyrite and pyrrhotite in the absence of conventional collectors. (1984).

[83] S. Kelebek. The effect of oxidation on the flotation behaviour of nickel–copper ores. In *XVIII Mineral Processing Congress. Sydney*, pages 999–1005, (1993).

[84] J. D. Miller, J. Li, J. C. Davidtz, and F. Vos. A review of pyrrhotite flotation chemistry in the processing of PGM ores. *Minerals Engineering*, 18(8):855–865, (2005). doi:10.1016/j.mineng.2005.02.011.

[85] T. Hirajima, H. Miki, G. P. W. Suyantara, H. Matsuoka, A. M. Elmahdy, K. Sasaki, Y. Imaizumi, and S. Kuroiwa. Selective flotation of chalcopyrite and molybdenite with H_2O_2 oxidation. *Minerals Engineering*, 100:83–92, (2017). doi:10.1016/j.mineng.2016.10.007.

[86] C. Djerassi, M. Gorman, F. X. Markley, and E. B. Oldenburg. Studies in Organic Sulfur Compounds. VII. 1 Lithium Aluminum Hydride Reduction of Xanthates to

Mercaptans. Synthesis of Substituted β-Mercaptoethanols. *Journal of the American Chemical Society*, 77(3):568–571, (1955).

[87] H. R. Manouchehri. Pyrrhotite flotation and its selectivity against pentlandite in the beneficiation of nickeliferous ores: An electrochemistry perspective. *Mining, Metallurgy & Exploration & Exploration*, 31(2):115–125, (2014). doi:10.1007/bf03402420.

[88] V. Bozkurt, Z. Xu, and J. Finch. Pentlandite/pyrrhotite interaction and xanthate adsorption. *International Journal of Mineral Processing*, 52(4):203–214, (1998). doi:10.1016/S0301-7516(97)00072-0.

[89] M. Hodgson and G. E. Agar. Eilectrochemical investigations into the flotation chemistry of pentlandite and pyrrhotite: process water and xanthate interactions. *Canadian Metallurgical Quarterly*, 28(3):189–198, (1989).

[90] Y. Zhang, Z. Cao, Y. Cao, and C. Sun. FTIR studies of xanthate adsorption on chalcopyrite, pentlandite and pyrite surfaces. *Journal of Molecular Structure*, 1048: 434–440, (2013). doi:10.1016/j.molstruc.2013.06.015.

[91] F. F. Lins, A. Middea, and R. Adamian. Processing of hydrophobic minerals and fine coal. In *Proceedings of the First UBC-McGill Bi-Annual International Symposium on Fundamentals of Mineral Processing*, page 61, (1995).

[92] S. Han, K. You, K. Kim, and J.-K. Park. Measurement of the attachment force between an air bubble and a mineral surface: Relationship between the attachment force and flotation kinetics. *Langmuir*, 35:9364–9373, (2019). doi:10.1021/acs.langmuir.9b00758.

[93] H. J. Butt and M. Kappl. *Surface and Interfacial Forces*. (2010). ISBN 9783527408498. doi:10.1002/9783527629411.

[94] Jacob N. Israelachvili. *INTERMOLECULAR AND SURFACE FORCES*, volume 52. (2015). ISBN 9780123751829.

[95] J. N. Israelachvili and R. M. Pashley. Measurement of the hydrophobic interaction between two hydrophobic surfaces in aqueous electrolyte solutions. *Journal of colloid and interface science*, 98(2):500–514, (1984).

[96] H. K. Christenson and P. M. Claesson. Direct measurements of the force between hydrophobic surfaces in water. *Advances in Colloid and Interface Science*, 91(3):391–436, (2001).

[97] J. L. Parker and P. M. Claesson. Forces between hydrophobic silanated glass surfaces. *Langmuir*, 10(3):635–639, (1994).

[98] E. E. Meyer, K. J. Rosenberg, and J. Israelachvili. Recent progress in understanding hydrophobic interactions. *Proceedings of the National Academy of Sciences*, 103(43): 15739–15746, (2006). doi:10.1073/pnas.0606422103.

[99] L. Xie, J. Wang, C. Shi, X. Cui, J. Huang, H. Zhang, Q. Liu, Q. Liu, and H. Zeng. Mapping the Nanoscale Heterogeneity of Surface Hydrophobicity on the Sphalerite Mineral. *Journal of Physical Chemistry C*, 121(10):5620–5628, (2017). doi:10.1021/acs.jpcc.6b12909.

[100] R. F. Tabor, A. J. Morfa, F. Grieser, D. Y. C. Chan, and R. R. Dagastine. Effect of gold oxide in measurements of colloidal force. *Langmuir*, 27(10):6026–6030, (2011). doi:10.1021/la200166r.